The Effect of Stress on Limestone Permeability and Effective Stress Behavior of Damaged Samples

Fanbao Meng, Patrick Baud, Hongkui Ge, Teng-fong Wong

AGU100 ADVANCING EARTH AND SPACE SCIENCE

JGR Solid Earth

RESEARCH ARTICLE
10.1029/2018JB016526

Special Section:
Physical Properties of Rocks, Friction and Fracturing: the Walsh Volume

The Effect of Stress on Limestone Permeability and Effective Stress Behavior of Damaged Samples

Fanbao Meng[1,2], Patrick Baud[3], Hongkui Ge[2,4], and Teng-fong Wong[1]

[1]Earth System Science Programme, Faculty of Science, The Chinese University of Hong Kong, Hong Kong, [2]Unconventional Petroleum Research Institute, China University of Petroleum, Beijing, China, [3]Institut de Physique du Globe de Strasbourg, (UMR 7516 CNRS, Université de Strasbourg/EOST), Strasbourg, France, [4]Faculty of Petroleum, China University of Petroleum-Beijing at Karamay, Karamay, China

Abstract The evolution of permeability and its effective stress behavior is related to inelastic deformation and failure mode. This was systematically investigated in Indiana and Purbeck limestones with porosities of 16% and 14%, respectively. High-pressure compression tests were conducted at room temperature on water-saturated samples. At relatively high confinement shear-enhanced compaction was observed to initiate at a critical stress, accompanied by significant permeability reduction of up to a factor of ~3. Overall, the permeability reduction due to inelastic compaction in our limestones is smaller than that observed in sandstones. At relatively low confinement, dilatant failure was observed, which was accompanied by a decrease and increase of permeability in Indiana and Purbeck limestones, respectively. There seems to be a trend for the correlation between porosity and permeability changes to switch from positive to negative with increasing porosity. The void space of both limestones has significant proportions of macropores and micropores. The effective stress behavior of such a limestone with dual porosity has been documented to be different from the prediction for a microscopically homogeneous assemblage, in that its effective stress coefficients for permeability and pore volume change may attain values significantly >1. In contrast, our investigation of damaged samples consistently showed effective stress coefficients for both permeability and pore volume change with values <1. This suggests that the behavior in the damaged samples is akin to that of a microscopically homogeneous assemblage, possibly due to pervasive collapse of macropores that would effectively homogenize the initially bimodal pore size distribution.

Key Points:
- With the development of shear-enhanced compaction, a permeability reduction by up to a factor 3 was observed in two porous limestones
- Dilatant failure was accompanied by modest variations of permeability in two porous limestones
- Inelastic compaction changed significantly the effective stress behavior of limestones with dual porosity

Supporting Information:
- Supporting Information S1

Correspondence to:
F. Meng,
quanquanmfb@163.com

Citation:
Meng, F., Baud, P., Ge, H., & Wong, T.-f. (2019). The effect of stress on limestone permeability and effective stress behavior of damaged samples. *Journal of Geophysical Research: Solid Earth*, *124*, 376–399. https://doi.org/10.1029/2018JB016526

Received 8 AUG 2018
Accepted 4 JAN 2019
Accepted article online 5 JAN 2019
Published online 24 JAN 2019

1. Introduction

A fundamental understanding of tectonic deformation and fluid flow in carbonate formation is of importance in many crustal processes. Field observations have documented that the development of faults and deformation bands in carbonate rocks is significantly more complex than in clastic rocks, since a complicated interplay of shear localization, inelastic compaction, stylolitization, and mechanical twinning may be involved (e.g., Peacock & Sanderson, 1995; Tondi et al., 2006; Willemse et al., 1997). Laboratory studies have also shown that although the phenomenology of low-temperature brittle-ductile transition in porous carbonate and clastic rocks are qualitatively similar, fundamentally different micromechanical processes are operative in the two different rock types (Wong & Baud, 2012).

Carbonates contain about 60% of the world's oil reservoirs, and yet the characterization of carbonate reservoirs remains challenging because of their heterogeneity and complex microstructure (Sayers, 2008). The depositional environment and diagenesis exert significant genetic influence over the development of texture and fabric of a carbonate rock, and as a result the pore geometry can be very complex (Choquette & Pray, 1970). The pore size typically spans over a very broad range, with a distribution that is often bimodal, including a significant subset of microporosity that cannot be resolved under an optical microscope (Pittman, 1971). Laboratory studies of the elastic behavior (Baechle et al., 2008) and inelastic failure (Zhu et al., 2010) in porous carbonate rocks have indicated that a more realistic interpretation of the mechanical behavior would often require a dual porosity model.

Since crustal deformation is often coupled with fluid transport, it is important to understand the evolution of permeability with mechanical deformation and stress. Laboratory studies have shown that the evolutions in a compact and a porous rock follow distinct paths (Paterson & Wong, 2005; Wong & Zhu, 1999). Most porous

Table 1
Petrophysical Description of the Rocks Investigated in This Study

Limestone name	Origin	Structure	Porosity (%)	Composition	References
Purbeck	UK	Allochemical	13.8	80%: calcite, 20%: quartz	Brantut et al. (2014)
Indiana	USA	Allochemical	16.1	100% calcite	Vajdova et al. (2012)

rock data are for sandstones, which typically show, under high confinement, a significant reduction of permeability with the onset of shear-enhanced compaction (Heffer, 2002; Zhu & Wong, 1997). Similar investigations of permeability evolution in porous carbonate rocks are limited; nevertheless, the data of Yale and Crawford (1998) for a suite of carbonate rocks (with total porosities ranging from 14% to 42%) and more recent data of Dautriat et al. (2011) for Estaillades limestone (porosity 29%), Lisabeth and Zhu (2015) for Indiana limestone (porosity 16%), and Brantut et al. (2018) for Purbeck limestone (porosity 14%) show an overall trend of compaction-induced permeability that is qualitatively similar to the extensive data on sandstones.

Notwithstanding this similarity, there is a quantitative difference between the permeability evolution, in that whereas in a sandstone the permeability reduction induced by inelastic compaction can be up to 2 orders of magnitude, that observed in a porous carbonate rock tends to be significantly less, typically less than an order of magnitude. Given that pore collapse is the dominant compaction mechanism in both types of porous sedimentary rocks, why does it lead to permeability reductions in sandstones and limestones that differ by order of magnitude? The first goal of the present work is to address this question by a systematic investigation of stress-dependent permeability in two limestones and its connection with the preexisting pore geometry, stress-induced damage and micromechanics of inelastic compaction.

Laboratory measurements on granular materials, crystalline rocks, and sandstones have shown that under low confinement, the onset and development of dilatancy are accompanied by either a moderate enhancement or reduction of permeability, depending on its initial porosity (Wong & Zhu, 1999). Since there is a paucity of laboratory data on the evolution of permeability with dilatant failure in carbonate rocks, it is unclear whether they will follow the same trend as the other rock types. Accordingly, the second objective of this study is to fill in the data gap, conduct systematic investigation in the brittle faulting regime, and establish a connection of permeability evolution with the micromechanics of dilatancy and shear localization.

Table 2
List of Symbols Used in This Study

Symbol	Description
P_c	Confining pressure
P_p	Pore pressure
P_{TE}	Terzaghi effective pressure, $P_c - P_p$
e_ϕ	Relative pore volume change
P^*	Critical stress for the onset of inelastic compaction under hydrostatic conditions
C'	Critical stress for the onset of dilatancy
C^*	Critical stress for the onset of shear-enhanced compaction
$C^{*\prime}$	Critical stress for the transition from shear-enhanced compaction to dilatancy
κ	Effective stress coefficient for permeability
β	Effective stress coefficient for pore volume change
α	Effective stress coefficient for axial strain
ξ	Change in permeability from dilatancy to peak stress
n	Sensitivity parameter of permeability to porosity (David et al., 1994)
γ	Sensitivity parameter of permeability to stress (David et al., 1994)
β_ϕ	Pore compressibility
K	Bulk modulus of the rock in Berryman's model (Berryman, 1992a, 1992b)
$K^{(1)}$	Bulk modulus of constituent 1 in Berryman's model (Berryman, 1992a, 1992b)

The applied stress field and pore pressure both exert significant influence over the hydromechanical attributes of a porous rock. The dependence of these attributes (including mechanical failure, deformation and fluid transport) on the interplay of applied stresses and pore pressure is collectively referred to as the "effective stress behavior." Mechanical failure has been observed to follow Terzaghi's effective stress law, such that the applied mean stress and pore pressure exert equal and opposite effects on the mechanical strength, and accordingly the effective stress coefficient for this property has a typical value of 1 (Baud et al., 2015; Paterson & Wong, 2005). In comparison, not as much is known concerning the effective stress behavior for permeability and (pore and bulk) deformation. Furthermore, existing data indicate that it can be more complicated than for mechanical failure. In this study we focused on Indiana and Purbeck limestones, the pore space of which has significant proportions of both macropores and micropores. In a recent analysis, Y. Wang et al. (2018) have demonstrated that the effective stress behavior of such a limestone with dual porosity contradicts the prediction of poroelasticity for a microscopically homogeneous material that the effective stress coefficients for permeability, pore volume change, and bulk strain are always less than or equal to unity. They observed in three limestones with dual porosity that the effects of confining and pore pressures on both permeability and pore volume change were

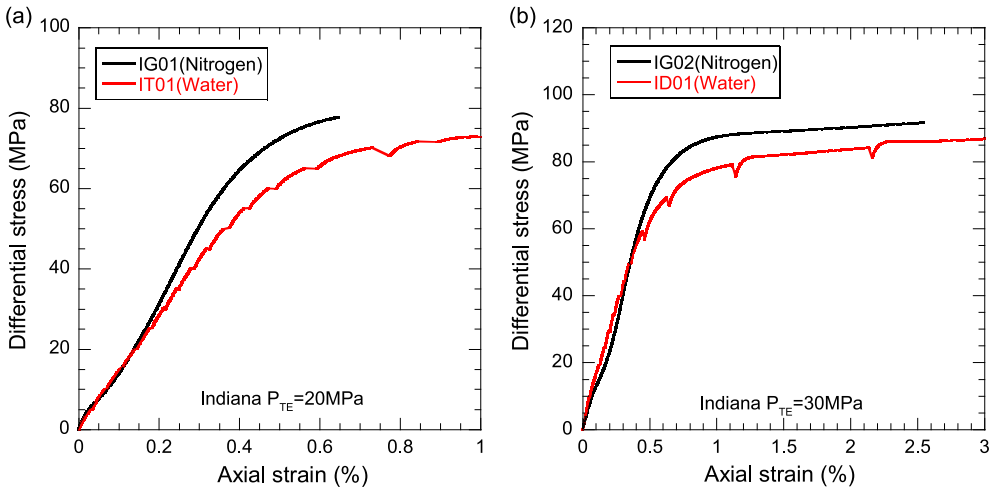

Figure 1. Mechanical data for samples of Indiana limestone saturated with nitrogen (black) and water (red). Differential stress as a function of axial stress for samples deformed at effective pressures of 20 MPa (a) and 30 MPa (b).

such that the effective stress coefficients were greater than unity, which implies that a change of pore pressure can exert a disproportionate control over the evolution of permeability and pore volume, with significant impact on the transport and storage of fluid in a carbonate reservoir or fault zone. Given that inelastic deformation is expected to modify the pore space and permeability and very little is known on the effect of such damage on the effective stress behavior, the third objective of this study is to follow up on this recent observation and address the question: To what extent will damage induced by inelastic

Table 3
Basic Physical Information and Experimental Description of the Tested Limestones

Sample		Porosity (%)	Conditions	Maximum axial strain (%)	Comment
Indiana	IH01	15.42	Hydrostatic, $P_p = 5$ MPa		Hydrostatic loading beyond P^*
	IB01	15.74	$P_c = 10$ MPa, $P_p = 5$ MPa	1.2	Brittle failure with shear bands at angles of ~30° with respect to σ_1
	IB02	15.65	$P_c = 15$ MPa, $P_p = 5$ MPa	3.6	Brittle failure with conjugate shear bands at high angle of ~45° with respect to σ_1
	IT01	15.84	$P_c = 25$ MPa, $P_p = 5$ MPa	5.4	Transitional mode
	ID01	15.77	$P_c = 35$ MPa, $P_p = 5$ MPa	4.9	Cataclastic flow
	ID02	15.80	$P_c = 45$ MPa, $P_p = 5$ MPa	3.8	Cataclastic flow
	ID03	15.87	$P_c = 55$ MPa, $P_p = 5$ MPa	5.6	Cataclastic flow
	IE01	17.42	Hydrostatic, $P_p = 5$ MPa	0.3	Hydrostatic loading beyond P^*, then the effective stress behaviors of the damaged sample were studied after unloading
	IE02	16.01	Triaxial loading, $P_c = 5$ MPa, $P_p = 1$ MPa	0.36	Triaxial loading beyond C', then effective stress behaviors of the damaged sample were studied after unloading
	IE03	15.61	Triaxial loading, $P_c = 35$ MPa, $P_p = 5$ MPa	2	Triaxial loading beyond C^*, then effective stress behaviors of the damaged sample were studied after unloading.
	IE04	18.12	Hydrostatic		The effective stress behaviors of this undamaged sample were studied by Y. Wang et al. (2018)
Purbeck	PB01	13.95	$P_c = 15$ MPa, $P_p = 5$ MPa	1.4	Brittle failure with shear bands at angle of ~30° with respect to σ_1
	PT01	13.05	$P_c = 35$ MPa, $P_p = 5$ MPa	2.9	Transitional mode
	PD01	13.35	$P_c = 65$ MPa, $P_p = 5$ MPa	3.3	Cataclastic flow
	PD02	13.46	$P_c = 85$ MPa, $P_p = 5$ MPa	4.6	Cataclastic flow
	PE01	13.95	Hydrostatic, $P_p = 5$ MPa, then Triaxial loading, $P_c = 85$ MPa, $P_p = 5$ MPa	1.2	Hydrostatic loading to 85 MPa under the pore pressure of 5 MPa, then triaxial loading beyond C^*, then the effective stress behaviors of the damaged sample were studied
	PE'01	13.95	Hydrostatic		Effective stress behaviors of undamaged sample

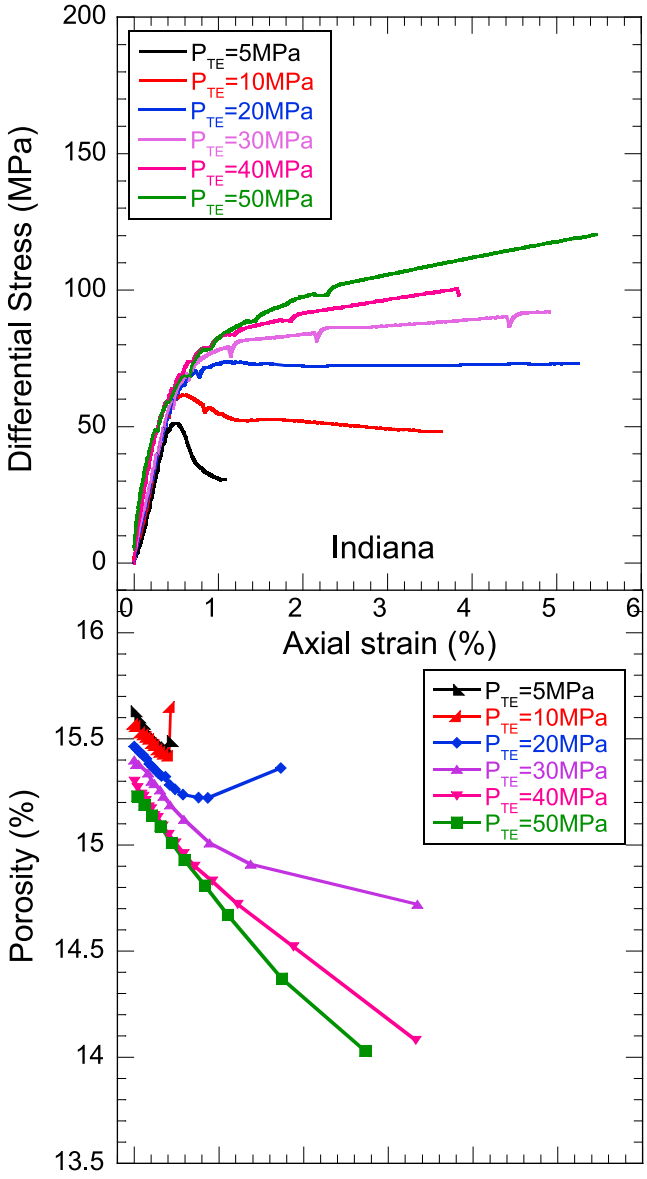

Figure 2. Mechanical data for water-saturated Indiana limestone. Differential stress and porosity were plotted versus axial strain for experiments performed at effective pressures between 5 and 50 MPa.

deformation in a porous limestone impact the effective stress behavior related to permeability, pore volume change, and strain?

Conventional triaxial compression experiments were conducted over a broad range of pressures to investigate the transition in failure mode from brittle faulting to cataclastic flow, as well as the evolution of permeability with this transition. We also investigated the effective stress behavior for permeability, pore volume change, and strain in limestone samples that had been hydrostatically and triaxially compacted to beyond the onset of pore collapse.

2. Experimental Procedure

2.1. Sample Materials

Table 1 lists the modal composition and porosity of Indiana and Purbeck limestones. The porosities were determined following the approaches of Y. Wang et al. (2018).

Indiana limestone is an allochemical limestone that is made up of primarily fossils and ooids. Whereas the interparticle space is occupied by relatively large macropores, numerous micropores are also found within the allochems, as well as along boundaries of allochems (Vajdova et al., 2012). Optical microscopy (Zhu et al., 2010), mercury porosimetry (Churcher et al., 1991; Tanino & Blunt, 2012; Y. Wang et al., 2018), X-ray computed tomography (CT) imaging (Ji et al., 2012), and nuclear magnetic resonance (NMR) relaxometry (Tanino & Blunt, 2012; Y. Wang et al., 2018) have been employed to characterize the pore structure in Indiana limestone in multiple scales. The hydromechanical and failure behaviors of Indiana limestone have also been investigated in some details (e.g., Coyner, 1984; Hart & Wang, 1995; Vajdova et al., 2004; Y. Wang et al., 2018).

Our Purbeck limestone samples were from the same block studied by Y. Wang et al. (2018). It is primarily made up of calcitic peloids, with multiplicity of polycrystalline quartz nodules distributed throughout the rock (Table 1). The macropores are mostly located between the cement and peloids, and micropores can be observed under the scanning electron microscope (SEM) to locate mostly within the peloids. Y. Wang et al. (2018) recently characterized this partitioning of the pore space using microscopy, mercury porosimetry, and NMR relaxometry. Permeability and sonic velocity, as well as their dependence on compaction in decane-saturated samples, were recently investigated by Brantut et al. (2018).

2.2. Mechanical Deformation and Permeability

Cored perpendicular to bedding, all our cylindrical samples had diameter of 40 mm. They were ground to parallel ends with a precision of ±10 μm. Nominal sample lengths were 80 and 40 mm for the triaxial and hydrostatic compression tests, respectively. The samples were saturated with deionized water (except in one experiment with nitrogen). As elaborated in supporting information Text S1 (Fatt, 1958; Lisabeth & Zhu, 2015; Y. Wang et al., 2018), the protocol of sample saturation was adopted to ensure that the fluid-rock system had attained equilibrium before initiating a mechanical test.

Technical details of the mechanical deformation and permeability measurements are described in supporting information Text S1. The jacketed samples were deformed at room temperature in the conventional triaxial configuration, with the axial stress $\sigma_1 > \sigma_2 = \sigma_3$. The confining pressures P_c ($= \sigma_3$) were fixed at values in the range from 10 to 85 MPa, while the pore pressure P_p was fixed at 5 MPa. The differences $P_c - P_p$ and $(\sigma_1 + 2\sigma_3)/3 - P_p$ will be referred to as the "Terzaghi effective pressure,"

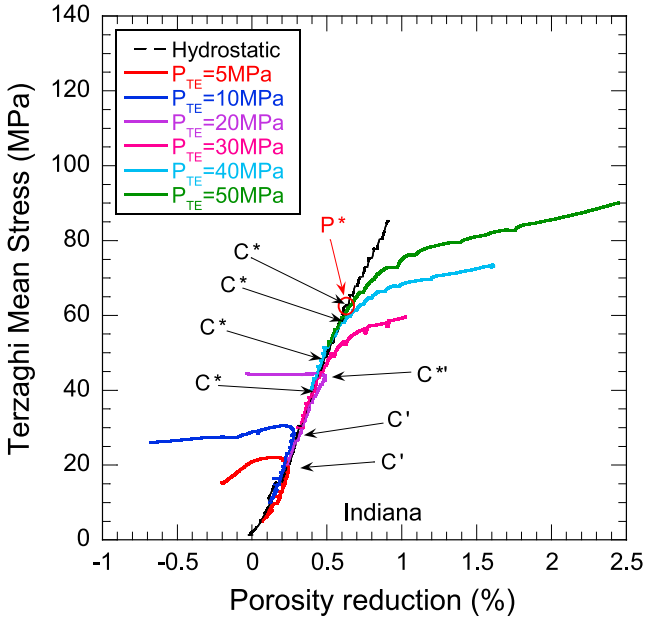

Figure 3. Terzaghi mean stress as a function of porosity reduction for water-saturated samples of Indiana limestone deformed at effective pressures between 5 and 50 MPa. For reference the hydrostatic data are shown as a black dashed line. Arrows in figure mark the critical stress states (onset of dilatancy *C′* in experiment at effective pressures of 5 and 10 MPa, onset of shear-enhanced compaction *C** in experiments performed at effective pressures of 30, 40, and 50 MPa, and transition from shear-enhanced compaction to dilatancy *C*′* in experiment at effective pressure of 20 MPa).

donated by "P_{TE}" and "Terzaghi mean stress," respectively. If the context is clear, we may drop the reference to Terzaghi and simply refer to these two quantities as effective pressure and effective mean stress, respectively. A list of the notations used in this study is provided in Table 2. After the

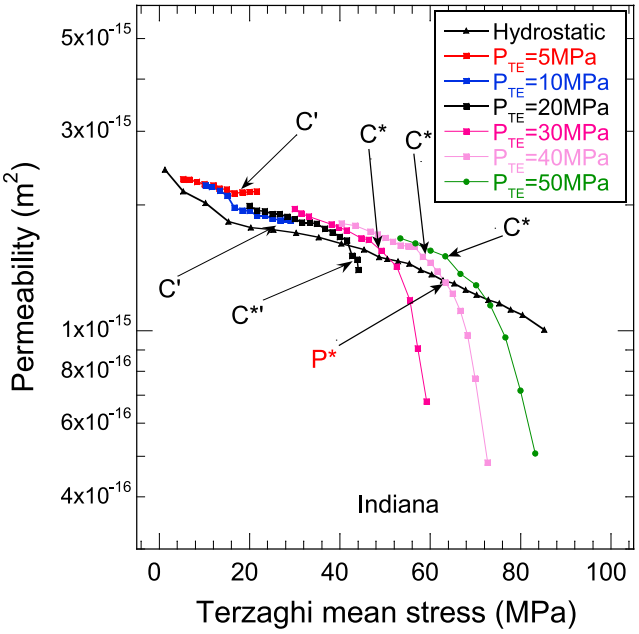

Figure 4. Permeability as a function of Terzaghi mean stress for samples of Indiana limestone deformed hydrostatically and triaxially. Arrows in figure mark the critical stress states (onset of dilatancy C′, onset of shear-enhanced compaction *C**, transition from shear-enhanced compaction to dilatancy *C*′*, and onset of inelastic deformation under hydrostatic conditions *P**).

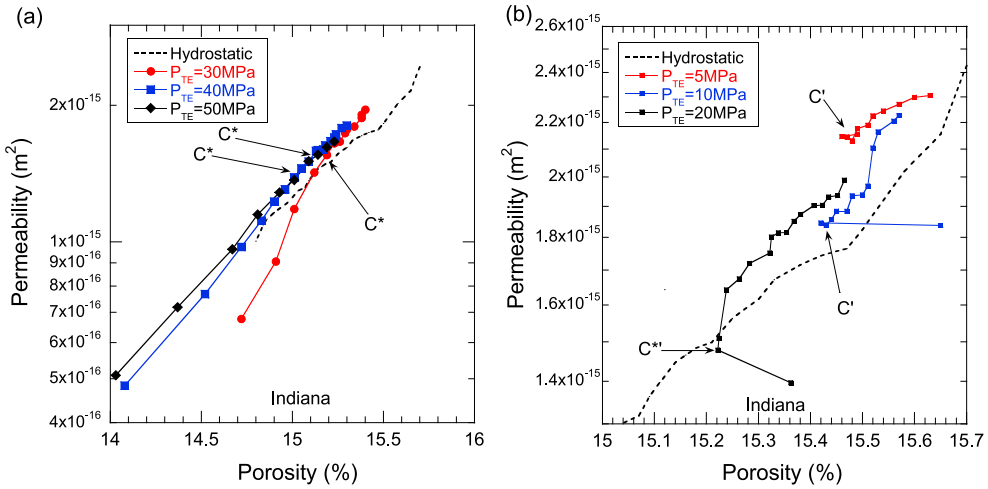

Figure 5. Permeability as a function of porosity for triaxially deformed samples of Indiana limestone during (a) cataclastic flow regime and (b) brittle faulting regime. For reference the data for the hydrostatic tests are shown as a dashed curve. The critical stress states C^*, $C^{*\prime}$, and C' are indicated by the arrows.

specific confining and pore pressures had been attained, the differential stress σ_1-σ_3 was increased at a nominal strain rate of 10^{-6}/s, which was sufficiently slow to ensure a fully "drained" condition.

At different stages of deformation the loading ram was locked and the permeability measured for hydraulic flow in the axial direction using the steady flow method. A constant flow rate 0.1 ml/min was maintained, and once a steady state in flow had been achieved, the measured difference in pore pressures between up and down stream was input into Darcy's law to calculate the permeability. For investigation of the effective stress behavior, the permeability, pore volume change, and bulk strain of a deformed sample were measured as functions of confining pressure at three different values of pore pressure; details of the procedure are provided in supporting information Text S1.

3. Hydromechanical Data

3.1. Evolution of Permeability With Stress and Failure Mode in Indiana Limestone

For Indiana limestone extensive mechanical data for dry samples have been presented by Vajdova et al. (2004). Our observations of the mechanical deformation and failure mode in water-saturated samples are qualitatively similar to the dry samples, but their mechanical strengths were somewhat lower. The water weakening effect is illustrated by comparing the stress-strain curves for Indiana limestone samples saturated with nitrogen (IG01 and IG02) and water (IT01 and ID01), respectively. The two sets of deformation experiments were conducted at effective pressures of 20 MPa (Figure 1a) and 30 MPa (Figure 1b), respectively. During strain hardening, at the same strain the stresses of the nitrogen-saturated sample were higher than the water-saturated sample by 10% or so.

Six triaxial and one hydrostatic compression experiments were conducted on water-saturated Indiana samples to measure permeability as a function of stress (Table 3). Mechanical data of the triaxially compressed samples are shown in Figure 2, with differential stress and porosity as functions of the axial strain. In Figure 3, we plot the Terzaghi mean stress as a function of porosity change of all seven samples. The hydrostat of sample IH01 is shown as the dashed line, on which the critical pressure P^* for the onset of pore collapse, corresponding to a deviation from poroelastic (linear) behavior, has been marked. The mechanical deformation of IB01 and IB02 at effective pressures of 5 and 10 MPa is characteristic of the brittle faulting regime. The differential stress attained a peak, after which it underwent strain softening and failed by the development of shear bands at angles of ~30° (Table 3). Dilatancy was observed to initiate at critical stresses C' as marked in Figure 3. The mechanical behavior of ID01, ID02, and ID03 at effective pressures of 30, 40, and 50 MPa, respectively, is characteristic of cataclastic flow.

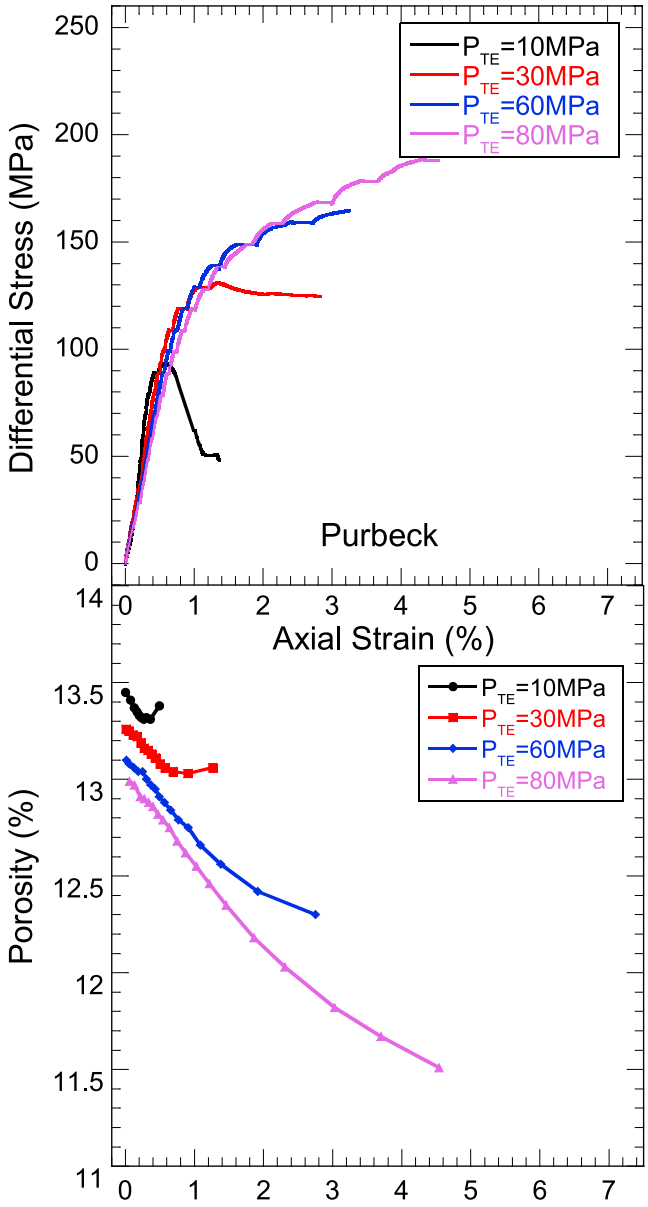

Figure 6. Mechanical data for water-saturated Purbeck limestone. Differential stress and porosity were plotted versus axial strain for experiments performed at effective pressures between 10 and 80 MPa.

The samples underwent monotonic strain hardening (Figure 2), and shear-enhanced compaction initiated at compactive yield stresses C^* as marked in Figure 3. The samples failed by diffuse compaction, without any signs of strain localization. At effective pressure of 20 MPa, a transitional mode of failure was observed in sample IT01. The peak stress level was almost flat (Figure 2), and the sample initially underwent a small amount of inelastic compaction and then switched to dilatancy at the critical stress $C^{*\prime}$ marked in Figure 3. Conjugate shear bands at relatively high angle of ~45° were observed in the failed sample.

The evolution of permeability with Terzaghi mean stress is shown in Figure 4. For hydrostatic compaction, the permeability of IH01 evolved in three stages. As the effective pressure increased initially to 15 MPa, its permeability decreased quite rapidly, likely related to the closure of preexisting microcracks. Permeability reduction then decelerated in the second stage, when the effective pressure increased to

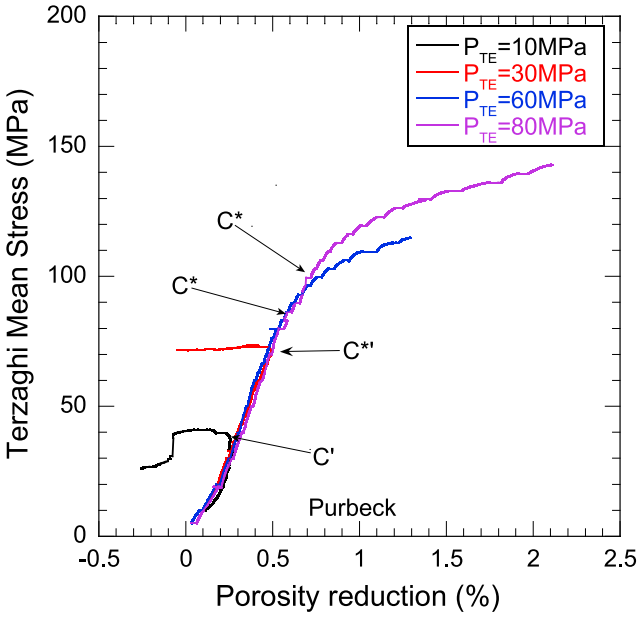

Figure 7. Terzaghi mean stress as a function of porosity reduction for water-saturated samples of Purbeck limestone deformed at effective pressures between 10 and 80 MPa. Arrows in figure mark the critical stress states (onset of dilatancy C' in experiment performed at effective pressure of 10 MPa, onset of shear-enhanced compaction C^* in experiments performed at effective pressures of 60 and 80 MPa, and transition from shear-enhanced compaction to dilatancy $C^{*\prime}$ in experiment at effective pressure of 30 MPa).

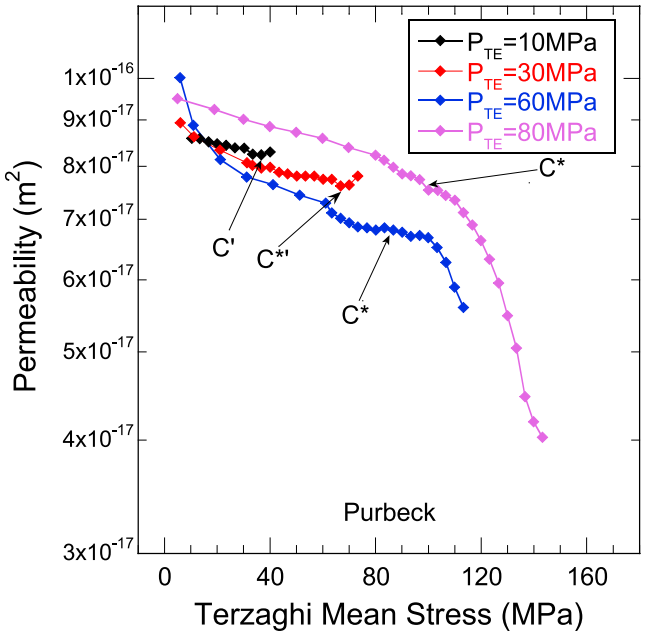

Figure 8. Permeability as a function of Terzaghi mean stress for triaxially deformed samples of Purbeck limestone. Arrows in figure mark the critical stress states (onset of dilatancy C', onset of shear-enhanced compaction C^*, and transition from shear-enhanced compaction to dilatancy $C^{*\prime}$).

near the critical pressure P^*. In the final stage with effective pressure beyond the critical value P^*, the permeability reduction became more rapid.

Under nonhydrostatic loading in the cataclastic flow regime, an accelerated reduction of permeability beyond the critical stress C^* was observed in each of the three samples (ID01, ID02, and ID03). The permeability of each sample decreased by a factor of between 3 and 4 for inelastic compaction up to 2%, (Figure 4), and permeability as a function of porosity has a positive slope (Figure 5a). A fundamentally different behavior was observed in the transitional regime. Beyond the critical stress $C^{*\prime}$, the permeability of IT01 was observed to decrease, even though the sample was dilating. Accordingly, its porosity and permeability changes were negatively correlated (Figure 5b). In the brittle faulting regime (IB01 and IB02), the permeability also showed a very slight decrease from the onset of dilatancy C' to near the peak stress (Figure 4), corresponding to a negative correlation between permeability and porosity changes that is close to 0.

3.2. Evolution of Permeability With Stress and Failure Mode in Purbeck Limestone

Four triaxial compression experiments were conducted on water-saturated Purbeck samples to measure permeability as a function of stress (Table 3). The mechanical data are shown in Figure 6, with differential stress and porosity as functions of the axial strain. The Terzaghi mean stress as a function of porosity change is also plotted in Figure 7. Mechanical deformation of PB01 at effective pressure of 10 MPa is characteristic of the brittle faulting regime, with an unstable stress drop in the postpeak stage and development of a shear bands at angle of ~30° (Table 3). Dilatancy was observed to initiate at critical stresses C' as marked in Figure 7. Mechanical behaviors of PD01 and PD02 at effective pressures of 60 and 80 MPa, respectively, are characteristic of cataclastic flow, with monotonic strain hardening (Figure 6), and shear-enhanced compaction beyond the yield stresses C^* as marked in Figure 7. The samples failed by diffuse compaction, without any signs of strain localization. At effective pressure of 30 MPa, a transitional mode of failure was observed in PT01, with very slight softening (Figure 6) that developed over a relatively large strain and was accompanied by significant dilatancy (Figure 7). Exterior appearance of the failed sample suggests the development of a complex network of shear bands at relatively high angle.

The evolution of permeability with Terzaghi mean stress is shown in Figure 8. In the cataclastic flow regime, an accelerated reduction of permeability beyond the critical stress C^* was observed in PD01 and PD02. For inelastic compaction up to 1.5%, the permeability reduced by a factor of up to 2 (Figure 8). In samples PB01 and PT01 deformed in the brittle faulting and transitional regimes, onset of dilatancy was accompanied by permeability increase (Figure 7). Accordingly, there is a positive correlation between permeability and porosity in all four samples (Figure 9).

3.3. Effective Stress Behavior for Permeability and Deformation in Damaged Limestone Samples

To investigate the influence of damage on effective stress behavior, three Indiana limestone and one Purbeck limestone samples were predeformed

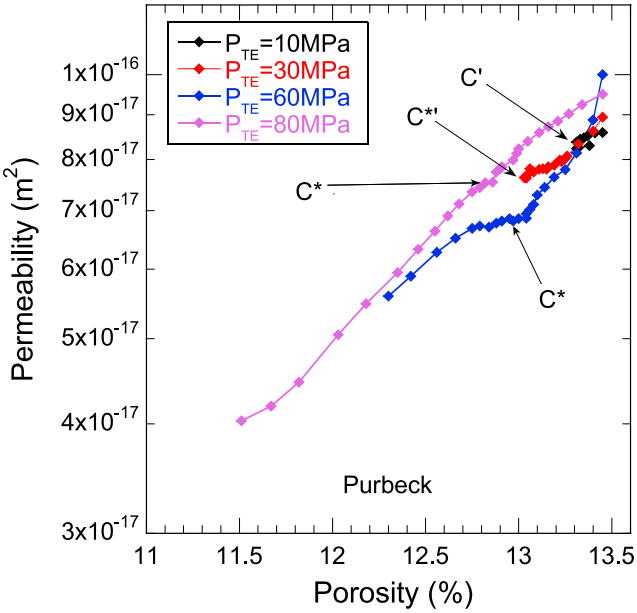

Figure 9. Permeability as a function of porosity for triaxially deformed samples of Purbeck limestone during cataclastic flow regime and brittle faulting regime. The critical stress states C^*, $C^{*\prime}$, and C' are indicated by the arrows.

inelastically to develop irreversible damage. Indiana limestone sample IE01 was hydrostatically compacted to beyond P^*, whereas IE02 and IE03 were triaxially compressed to beyond the critical stresses C' and C^*, respectively. The Purbeck limestone sample PE01 was triaxially compressed to beyond C^* (Table 3). The mechanical data for the pre-stressing of these four samples are presented as supporting information (Figures S1–S4). To characterize the effective stress behavior of the four damaged samples, the permeability, pore volume change, and bulk strain were measured as functions of confining pressure at three different values of pore pressure. The experimental data were used to constrain three effective stress coefficients: κ for permeability, β for pore volume change, and α for axial strain (Y. Wang et al., 2018). Mathematical definitions of these coefficients are elaborated in supporting information Text S2.

3.3.1. Effects of Confining and Pore Pressures on Permeability

We present in Figures 10a and 10b the data of permeability as a function of confining and pore pressures for Indiana and Purbeck limestones, respectively. For all four damaged samples, evolution of permeability was qualitatively similar. At a fixed pore pressure, permeability decreased with increasing confining pressure in an approximately linear trend. At a fixed confining pressure, permeability was observed to increase with increasing pore pressure. Overall, the effect of pore pressure on permeability change was smaller than that of confining pressure. This behavior in our damaged samples is fundamentally different from that for initially undamaged samples as documented by Y. Wang et al. (2018). Data for their intact samples showed that roles of the two pressures were reversed, with the pore pressure exerting a significantly stronger influence than confining pressure on the permeability.

We show in Figure 11 iso-permeability contours constrained by our data in the $P_c - P_p$ space. It can be seen that the contours are generally nonlinear, but as noted by Y. Wang et al. (2018) certain second-order features of the curvature may be artifacts due to our interpolation from limited data. The effective stress coefficient κ for our damaged limestone samples can be inferred from local slopes of the contours, which seem consistently smaller than 1. Among the three Indiana limestone samples, the hydrostatically compacted sample IE01 and shear-compacted sample IE03 were observed to have the highest and lowest values of κ, respectively.

To quantify the effect of confinement on κ, we adopted an approximate scheme (summarized in supporting information Text S2) to estimate the effective stress coefficient κ, which shows a moderate dependence on

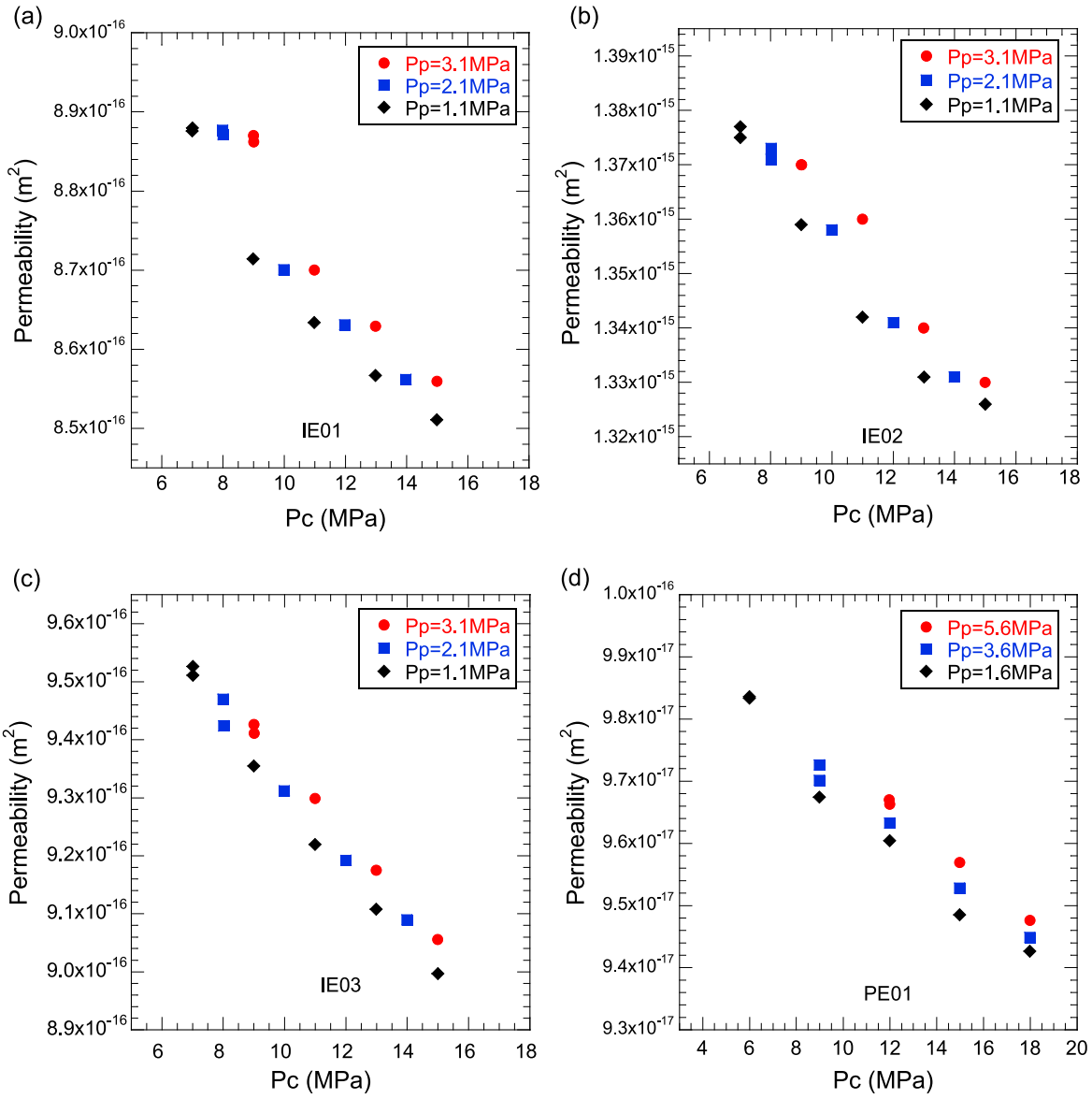

Figure 10. Permeability as a function of confining pressure for three different pore pressures for samples of Indiana limestone (a) IE01 hydrostatically compacted beyond P^*, (b) IE02 triaxially compressed beyond C', and (c) IE03 triaxially compressed beyond C^*, and sample PE01 (d) of Purbeck limestone triaxially compacted beyond C^*.

the confining pressure, with values consistently less than unity (Figure 12). It should be noted that a somewhat different behavior was observed in the sample IE01 (Figure 10a), with a nonlinear and relatively rapid decrease of permeability during the initial increase of confining pressure, possibly due to microcrack closure. For this sample if we exclude the data point for the lowest confining pressure, then the data follow a linear trend and we can apply the approximate scheme to evaluate the derivatives. For a similar reason the data points for the lowest confining pressures were not included in our latter analyses of pore volume change and axial strain.

For comparison we include in Figure 12 values of κ for two initially undamaged samples. Data for the Indiana limestone sample IE04 were presented by Y. Wang et al. (2018), who also investigated the effective stress behavior of Purbeck, Thala, and Leitha limestones. For Purbeck limestone they did not obtain satisfactory data on the strain, and we therefore decided in this study to conduct another experiment on a new sample PE'01. Y. Wang et al. (2018) concluded that for the three limestones (Indiana, Purbeck,

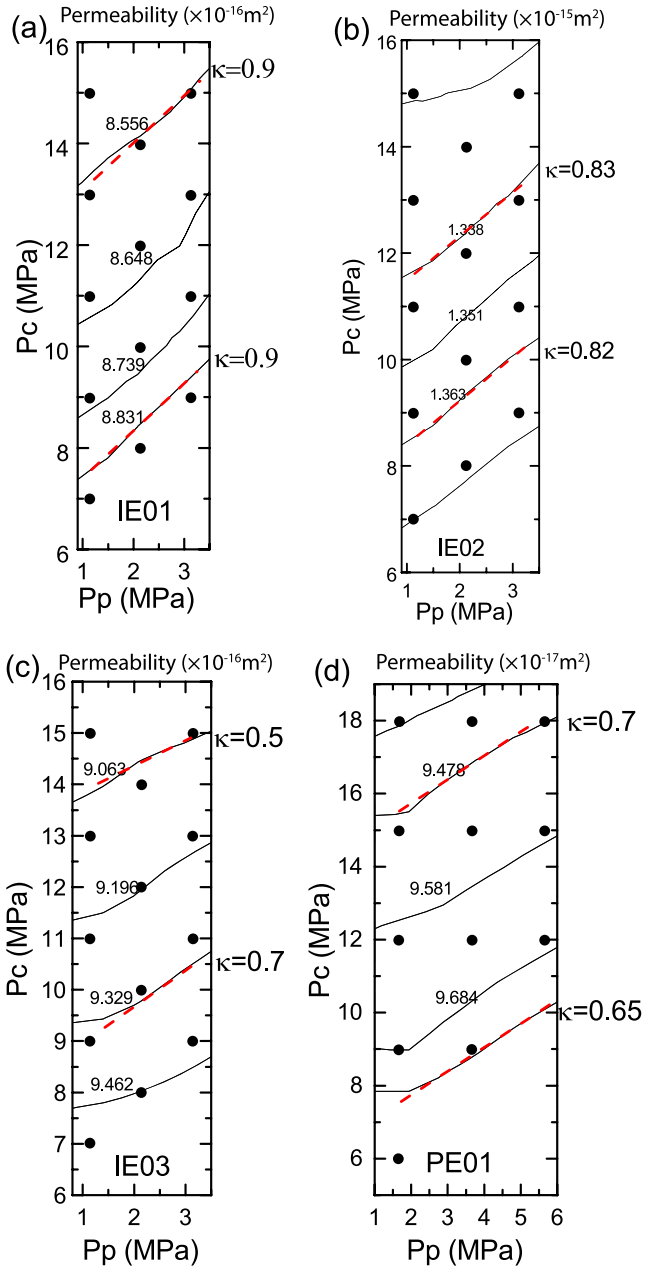

Figure 11. Iso-permeability contours (m^2) presented in a confining pressure-pore pressure space for samples of Indiana limestone (a) IE01 hydrostatically compacted beyond P^*, (b) IE02 triaxially compressed beyond C', and (c) IE03 triaxially compressed beyond C^*, and sample PE01 (d) of Purbeck limestone triaxially compacted beyond C^*.

and Thala) with dual porosity, their effective stress coefficient $\varkappa$ for permeability consistently had values >1. Highest values (up to ~5) were observed in Thala limestone, and lowest values (~1.3, comparable to our data here for PE'01) in Purbeck limestone. Comparison of the two sets of data in Figure 12 underscores the influence of damage on the effective stress behavior of a carbonate with double porosity. Whereas the coefficient $\varkappa$ typically has values greater than unity in an initially undamaged sample, the development of damage in the pore space tends to weaken the role of pore pressure relative to that of confining pressure in changing permeability. As a result the coefficient $\varkappa$ would decrease to a value less than unity.

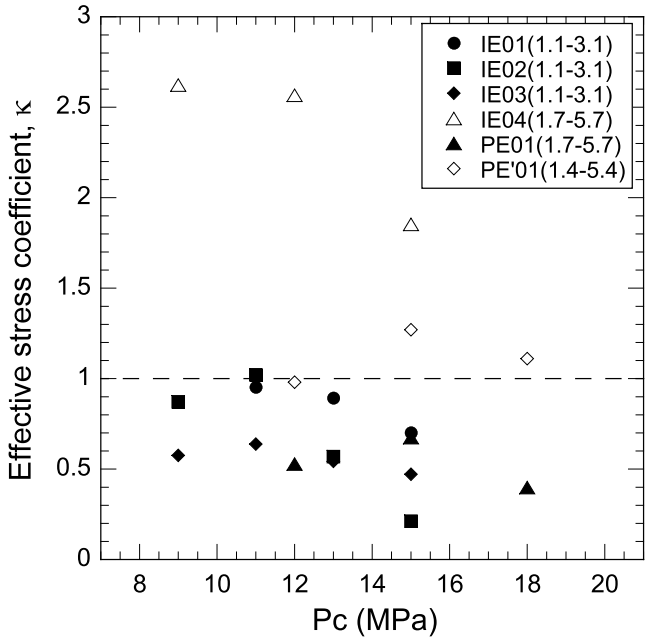

Figure 12. Effective stress coefficient κ as a function of confining pressure for samples of Indiana and Purbeck limestone. Damaged and undamaged samples are presented as closed and open symbols, respectively. For reference, the case $\kappa = 1$ is presented as a dashed line.

3.3.2. Effects of Confining and Pore Pressures on Pore Volume

The measured pore volume change δV_v was divided by the initial pore volume V_v to infer the relative pore volume change e_ϕ. We present in Figures 13a–13c and 13d data for e_ϕ as a function of confining and pore pressures in the damaged Indiana and Purbeck sandstone samples, respectively. The relative pore volume changes were on the order of 10^{-3} to 10^{-2} in the damaged samples. With increasing confining pressure, the pore volume decreased in an approximately linear trend at a given pore pressure. Changes in e_ϕ due to the interplay of confining and pore pressures were qualitatively similar to the results presented for the permeability evolution in the previous section, in that the effect of pore pressure was small relative to that of confining pressure. Again, the effective stress behavior is fundamentally different from that for the initially undamaged samples as documented by Y. Wang et al. (2018), who observed that pore pressure exerted a stronger influence than confining pressure on the pore volume change.

Figure 14 shows contours of constant e_ϕ based on our data and plotted on the $P_c - P_p$ space. The effective stress coefficient β for pore volume inferred from slopes of the contours was inferred to be smaller than 1 for all four damaged samples. The scheme used earlier for permeability was also adopted to analyze the dependence of coefficient β on the confining pressure (Figure 15). As before the coefficient β for the damaged samples is inferred to have moderate dependence on the confining pressure, and consistently less than unity. For comparison we include in the figure values of β determined for the initially undamaged samples IE04 and PE'01, both with values >1. Again, the contrast underscores the influence of damage on lowering the effective stress coefficients of these two limestones with dual porosity.

3.3.3. Effects of Confining and Pore Pressures on Axial Strain

Figure 16 shows data for axial strain of the four damaged samples as a function of confining and pore pressures. The strains were on the order of 10^{-4} to 10^{-3} in the damaged samples. At a fixed pore pressure, axial strain increased almost linearly with confining pressure. Overall, the effect of pore pressure on strains was small relative to that of the confining pressure. Contours of constant axial strain as constrained by our data are plotted on the $P_c - P_p$ space in Figure 17. Local slopes of these contours indicate that the inferred values of effective stress coefficient α for axial strain consistently have values less than unity. Figure 18 presents the evolution of α with confining pressure inferred using the same procedure as before for permeability and pore volume. For comparison we include in the figure values of α determined for the initially undamaged samples IE04 and PE'01, which are also <1. No clear variation of α with confining pressure could be observed. In contrast to permeability and pore volume change, comparison of the two sets of data here does not indicate any systematic effect of damage on the effective stress behavior of these two limestones with dual porosity, in that for both initially undamaged and damaged samples of Indiana and Purbeck limestones we observed values of α less than unity.

4. Discussion

Our investigation of the permeability and porosity changes in Indiana and Purbeck limestones over a broad range of pressure conditions has elucidated the evolution of these two hydromechanical properties with stress and failure mode associated with the low-temperature brittle-ductile transition. Yale and Crawford (1998) investigated the permeability evolution in a suite of carbonate rocks, but due to the variability among their samples, it was difficult to isolate the influences of stress, porosity change, and failure mode. The investigation of Dautriat et al. (2011) on Estaillades limestone has provided new insights into permeability anisotropy and the dependence on loading paths. Lisabeth and Zhu's (2015) study of Indiana limestone has highlighted the chemical effect of water and temperature on failure and permeability evolution. However, because the range of confining pressure in both studies was

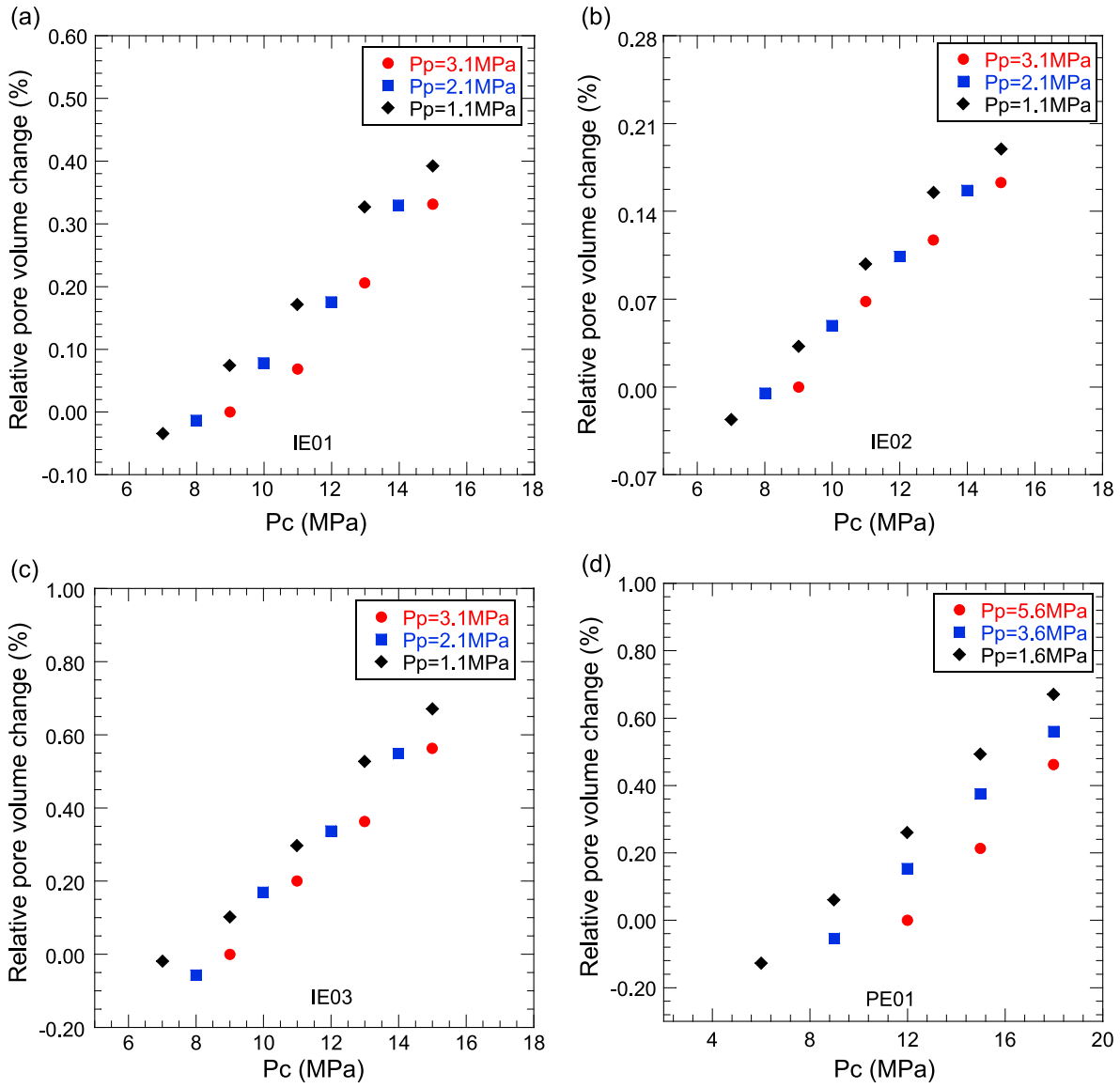

Figure 13. Relative pore volume change as a function of confining pressure for three different pore pressures for samples of Indiana limestone (a) IE01 hydrostatically compacted beyond P^*, (b) IE02 triaxially compressed beyond C', and (c) IE03 triaxially compressed beyond C^*, and sample PE01 (d) of Purbeck limestone triaxially compacted beyond C^*.

somewhat limited, it is difficult to draw broader conclusions on the influence of stress and failure mode. Brantut et al. (2018) investigated the evolutions of sonic velocity and permeability in Purbeck limestone over a broad range of confinement. However, their permeability data (acquired using the pore pressure oscillation technique) involve significant scatter, rendering it difficult to draw more definitive conclusions on the subtle changes of permeability that accompany dilatancy.

On the basis of extensive laboratory data on five sandstones with porosities ranging from 15% to 35%, Zhu and Wong (1997) proposed a conceptual model for the coupling of deformation and fluid transport in the form of a deformation-permeability map for siliciclastic rocks. Previous studies (Dautriat et al., 2011; Lisabeth & Zhu, 2015; Yale & Crawford, 1998) implicitly assumed that a similar model is applicable to porous carbonate rocks, even though several aspects have yet to be characterized experimentally. Our systematic investigation here fills in important gaps on our understanding of the deformation-permeability map, particularly on quantitative correlation among permeability, porosity, and stress in the cataclastic flow regime, as well as qualitative behavior in the brittle faulting and transitional regimes.

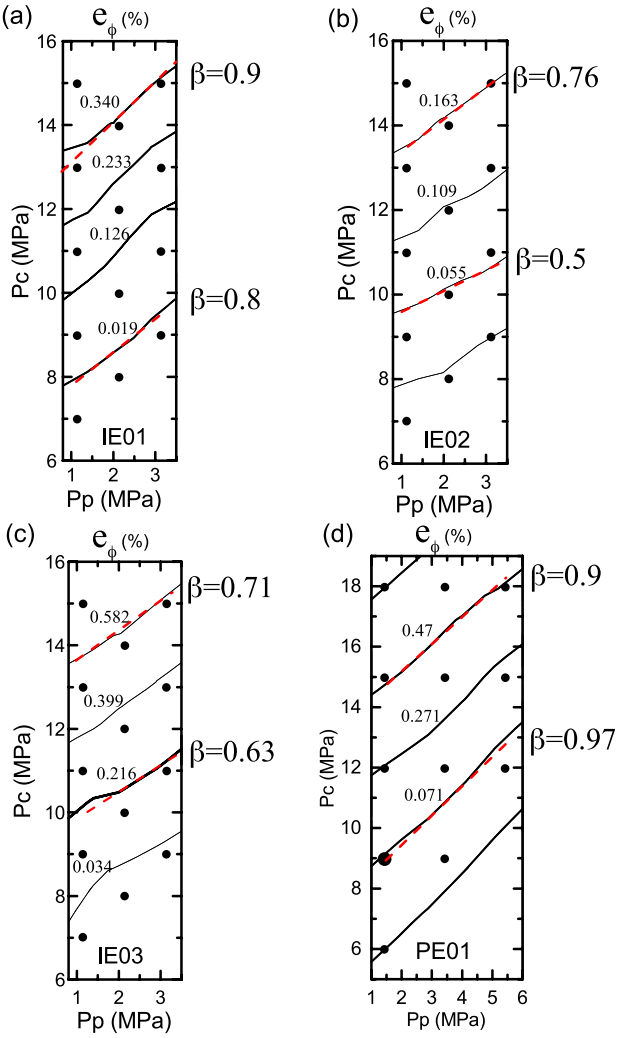

Figure 14. Iso-pore volume change contours presented in a confining pressure-pore pressure space for samples of Indiana limestone (a) IE01 hydrostatically compacted beyond P^*, (b) IE02 triaxially compressed beyond C', and (c) IE03 triaxially compressed beyond C^*, and sample PE01 (d) of Purbeck limestone triaxially compacted beyond C^*.

4.1. Mechanical Compaction and Permeability Reduction in Porous Limestones

According to the conceptual model, permeability and porosity changes for cataclastic flow closely track one another, with the compactive yield stress C^* mapping out a cap in stress space that represents a boundary between two different types of permeability evolution. Such caps for our water-saturated Purbeck and Indiana samples are shown in Figures 19a and 19b, respectively. Similar to what have been observed in a variety of porous rocks (Wong & Baud, 2012), these caps are approximately elliptical in shape. For comparison we include in Figure 19a the data of Brantut et al. (2014, 2018) for water-saturated samples and decane-saturated samples of Purbeck limestone. However, comparison of published results and our new data is not totally straightforward. In our study, samples were deformed at a strain rate of 10^{-6}/s and the loading ram had to be stopped multiple times for the measurement of permeability, and because these samples were subjected to numerous cycles of stress relaxation, their strengths are expected to be somewhat lower that those that were continuously deformed by Brantut et al. (2014, 2018) at a constant and faster strain rate of 10^{-5}/s. Moreover, the water-saturated samples deformed by Brantut et al. (2014) were smaller than those used in our study and those of Brantut et al. (2018). While it has been shown by previous studies that larger samples tend to be weaker in the brittle regime (Paterson & Wong, 2005), the impact of sample size on the onset of shear-enhanced compaction is to our knowledge still unclear. Despite these limitations, Figure 19a suggests some water weakening in our samples. This was confirmed by the results of an additional hydrostatic test performed at EOST Strasbourg that lead to a value of P^* of 120 MPa (Figure 19a) slightly less than the 128 MPa reported for a decane-saturated sample (Brantut et al., 2018). These observations are in line with recent results showing some significant reduction of both the uniaxial compressive strength of some porous limestones from Bure (France; Baud et al., 2016) and of the onset of shear-enhanced compaction in Saint-Maximin limestone (Baud, Exner, et al., 2017) in presence of water. Also, for comparison we include in Figure 19b the data of Vajdova et al. (2004) for nominally dry samples of Indiana limestone deformed in constant strain rate. Given the stress relaxation cycles and water weakening, one would expect the compactive yield stresses of our samples to be lower than those of Vajdova et al. (2004), if the porosities of both suites of samples are comparable. However, because their samples were from a block of significantly higher porosity (~20%), the corresponding yield stresses of Vajdova et al. (2004) were lower than ours. More systematic comparisons should be done in the future to quantify precisely water weakening in porous limestone.

Our data here for the two porous limestones (Figures 4 and 8) show that their behavior is qualitatively similar to that for sandstones. Before the critical stress C^* is attained, permeability and porosity both decrease with increasing hydrostatic loading, but the evolution is basically independent of the deviatoric stress field. However, at stress levels beyond C^* permeability and porosity changes are sensitively dependent on not only the hydrostatic loading but also the deviatoric loading. Loading beyond the cap would result in an accelerated decrease of permeability with increasing stress. In out experiments, permeability decreased by a factor of between 2 and 4 for inelastic compaction up to 2%.

Though significant, such permeability reductions are relatively small in comparison to corresponding changes in sandstones, which can be up to 1 or 2 orders of magnitude (Zhu & Wong, 1997). To quantify this difference, we follow David et al. (1994) to analyze the sensitivity of permeability to porosity and stress with

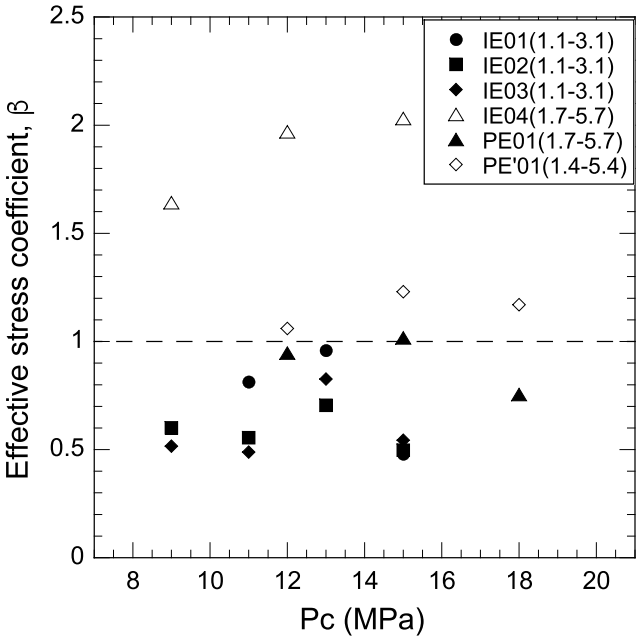

Figure 15. Effective stress coefficient β for relative pore volume change as a function of confining pressure. Damaged and undamaged samples are presented as closed and open symbols, respectively. For reference, the case $\beta = 1$ is shown as a dashed line.

the two parameters n and γ, respectively. For porosity dependence, a power law is used to empirically describe the permeability evolution:

$$k/k_o = (\phi/\phi_o)^n \tag{1a}$$

Here k and k_o are permeability values for samples with porosity ϕ and reference porosity ϕ_o, respectively. To estimate the exponent n, we compile and plot our data of permeability versus porosity, both on logarithmic scales (Figure 20a). For comparison, we also include data for selected sandstones compiled by David et al. (1994). They focused on hydrostatic compression and observed that there is a trend for the exponent value to increase as effective pressure increases to beyond the critical value P^*. Zhu and Wong (1997) subsequently showed a similar increase of n at stress states beyond C^*. Compilation of David et al. (1994) indicated values of n for elastic and inelastic compression of porous sandstones to range from 1.9 to 25.4 (Figure 20b). In comparison, corresponding values for Purbeck limestone are significantly smaller with $n < 8$ (Figure 20b). Values of n for Indiana limestone are larger and in the range reported on porous sandstones. For Indiana samples deformed beyond the yield point, n was around 15, in the range reported by Yale (1984) for tight sandstones.

If permeability is k at the Terzaghi mean stress σ_{eff} and that at a reference effective pressure P_o (by convention the atmospheric pressure) is k_o, this empirical relation was used by David et al. (1994) to analyze the stress sensitivity of permeability:

$$k = k_o \exp[-\gamma(\sigma_{\text{eff}} - P_o)] \tag{1b}$$

They primarily focused on hydrostatic loading, but since we here generalize the analysis to also include non-hydrostatic loading, the Terzaghi mean stress instead of effective pressure is considered. The coefficient γ can be estimated from the slope of a log-linear plot of permeability versus Terzaghi mean stress (Figures 4 and 8). In porous sandstones there is an overall trend for γ to increase to a peak at a stress level just beyond the cap (Zhu & Wong, 1997). From the compilation of David et al. (1994), values of γ for elastic and inelastic compression of porous sandstones range from 0.002 to 0.02 MPa^{-1} (Figure 20b). The values for our two limestones fall in the same range but more on the lower end (Figure 20b). We note that significantly larger values were obtained for samples of Indiana limestone deformed beyond the yield point.

4.2. Effect of Macropore Collapse on Permeability

Although the porosities of our porous limestones are significantly smaller than those of sandstones, the two coefficients n and γ of are positively correlated in both rock types. David et al. (1994) suggested that such a positive correlation can be explained by noting that the two coefficients are related by

$$\gamma = -\frac{n}{\phi}\frac{\partial \phi}{\partial \sigma_{\text{eff}}} = n\beta_\phi \tag{2}$$

where β_ϕ denotes the pore compressibility, which must be positive. Accordingly, a high γ/n ratio signifies a relatively compliant pore space. David et al. (1994) concluded that the data for porous sandstones can be bracketed by two linear boundaries that correspond to $\beta_\phi = 4.4 \times 10^{-4}$ to 3.3×10^{-3} MPa^{-1}. It can be seen in Figure 20b that most of our data for porous limestones are also bracketed by these boundaries, with the implication that their pore compressibility is comparable to that of porous sandstones. This is in contrast to tight and fractured rocks, typically with significantly higher γ/n ratios likely due to the large compliance of microcracks and fractures.

However, it should be noted that the pore compressibility here reflects the global porosity reduction which, in a limestone with dual porosity, would predominately derive from compaction of the macropores. For the

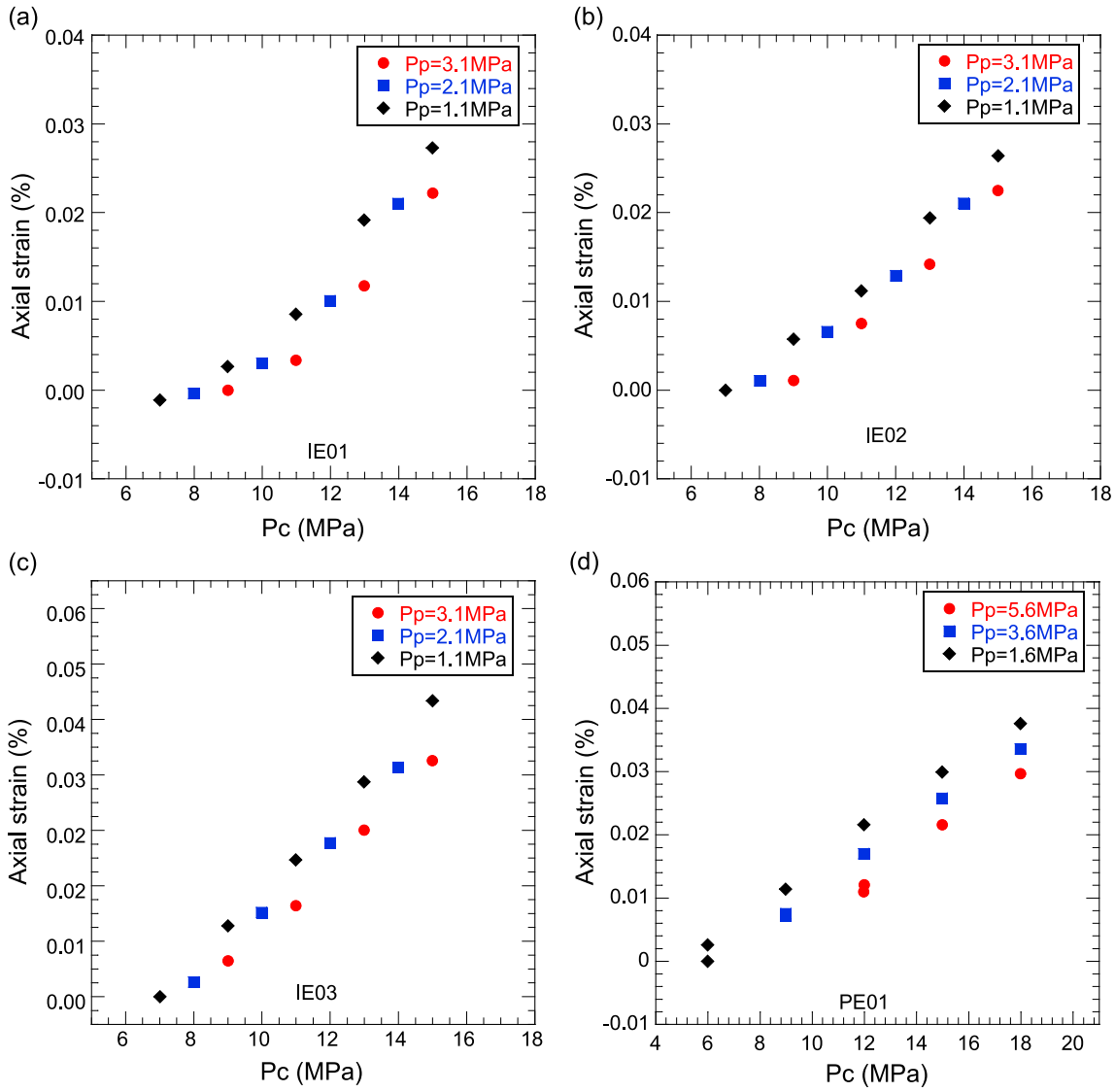

Figure 16. Axial strain as a function of confining pressure for three different pore pressures for samples of Indiana limestone (a) IE01 hydrostatically compacted beyond P^*, (b) IE02 triaxially compressed beyond C', and (c) IE03 triaxially compressed beyond C^*, and sample PE01 (d) of Purbeck limestone triaxially compacted beyond C^*.

inelastic case, the partitioning of local compaction between macropores and micropores can be inferred from microstructural observations on damaged samples. Optical and SEMs (Vajdova et al., 2012), as well as X-ray micro-CT (Ji et al., 2012), were used to characterize the pore size distributions of undamaged and inelastically deformed samples of Indiana limestone. Indeed, these observations have underscored the predominate contribution of macropore collapse toward the inelastic compaction. Brantut et al. (2018) performed SEM observations on deformed samples of Purbeck limestone and reported qualitatively similar behavior.

Even though contribution of the micropores to the overall compaction may be small, a number of observations and modeling studies have suggested that they likely have a more significant control as far as permeability is concerned. Ji et al. (2012) inferred from CT imaging that the clustering of macropores in Indiana limestone seems insufficient to provide a percolative conduit, and accordingly, the fluid transport and permeability must leverage relatively narrow conduits connected to micropores. This inference is consistent with the two inflection points typically observed in the mercury porosimetry

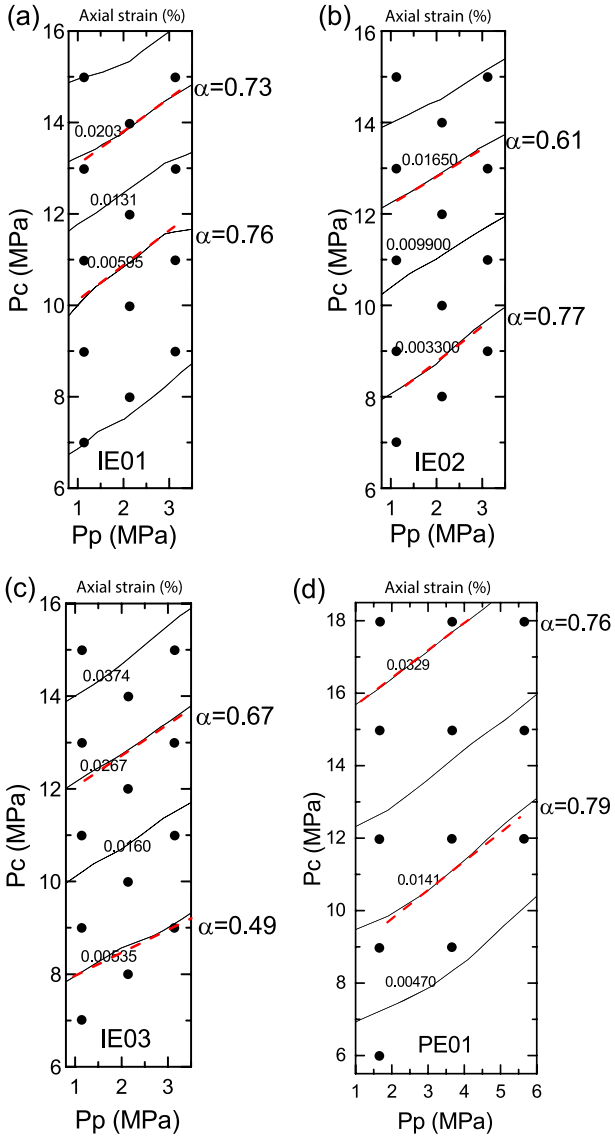

Figure 17. Iso-axial strain presented in a confining pressure-pore pressure space for samples of Indiana limestone (a) IE01 hydrostatically compacted beyond P^*, (b) IE02 triaxially compressed beyond C', and (c) IE03 triaxially compressed beyond C^*, and sample PE01 (d) of Purbeck limestone triaxially compacted beyond C^*.

data for a carbonate with double porosity (Figure 21). In percolation simulations of carbonate rocks, this critical role of micropores in controlling permeability has also been underscored (e.g., Al-Kharusi & Blunt, 2008; Bauer et al., 2011, 2012).

Nevertheless, it should be noted that role of the micropores may vary in limestones with different pore structures. Baud, Schubnel, et al. (2017) recently investigated the mechanical behavior, failure mode, and transport properties of Leitha limestone, the pore space of which is dominated by macropores, with negligible microporosity. Accordingly, the contribution of micropores toward permeability is also minimal. Even for a limestone with dual porosity, a percolative backbone of macropores may exist if the total porosity is relatively high. Indeed, the micro-CT data of Ji et al. (2015) indicate the existence of such a backbone in Majella limestone with 31% porosity. Inelastic compaction in this case could possibly result in more spectacular permeability decrease if this backbone was to be disconnected. However, this would need to be confirmed by further studies.

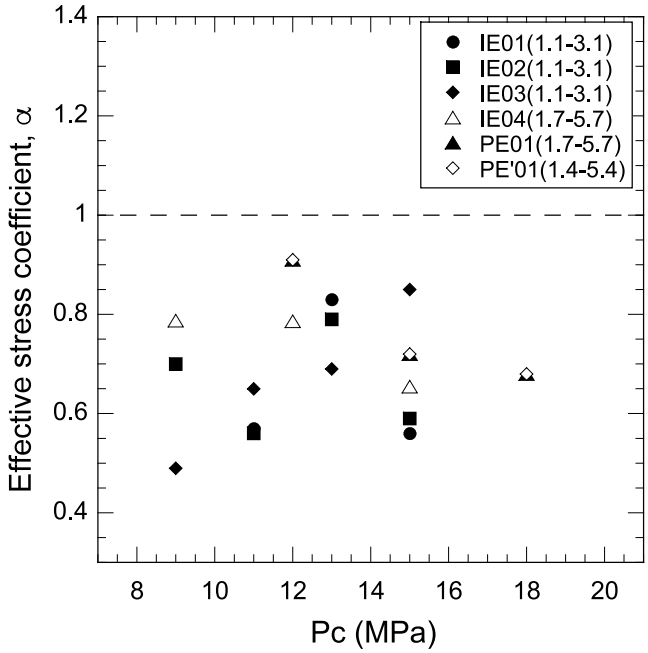

Figure 18. Effective stress coefficient α as a function of confining pressure. Damaged and undamaged samples are presented as closed and open symbols, respectively. For reference, the case $\alpha = 1$ is shown as a dashed line.

4.3. Permeability Change in a Dilating Limestone

In the brittle faulting regime, the correlation between porosity and permeability changes during dilatant failure can be characterized by the permeability change factor ξ that Zhu and Wong (1997) and Wong and Zhu (1999) proposed:

$$\xi = \frac{k(\text{peak})}{k(c')} - 1 \tag{3}$$

Here $k(C')$ and k (peak) denote the permeabilities at the onset of dilatancy and peak stress, respectively. We compile in Table 4 values of ξ evaluated from our laboratory (Figures 5b and 9) and published data. To our knowledge, there have been two related studies on porous limestones: Dautriat et al. (2011) investigated the Estaillades limestone, and they presented one set of data on permeability evolution in a sample triaxially compressed at confining and pore pressures of 3 and 1 MPa, respectively. It showed dilatancy and failed by brittle faulting, that was accompanied by permeability reduction (Table 4). Regnet et al. (2015) presented permeability data for two Oolithe Blanche limestones samples, triaxially compressed at confining and pore pressures of 28 and 5 MPa, respectively. In each sample the permeability showed a very slight increase from the onset of dilatancy C' to near the peak stress (Table 4). Overall, there is a trend for the value of ξ to switch from positive to negative as porosity increases to beyond 15% or so.

For comparison we include in Figure 22 permeability change factors for other lithified rocks and granular material compiled by Wong and Zhu (1999), who concluded that the correlation between porosity and permeability changes is positive for a variety of geomaterials with porosities less than ~15%. The correlation switches to negative for more porous aggregates. Our compilation shows that porous limestones follow a similar qualitative trend, albeit with ξ value significantly smaller than most other rocks. In porous sandstones, that permeability would decrease in a dilatant rock can be explained by the interplay between

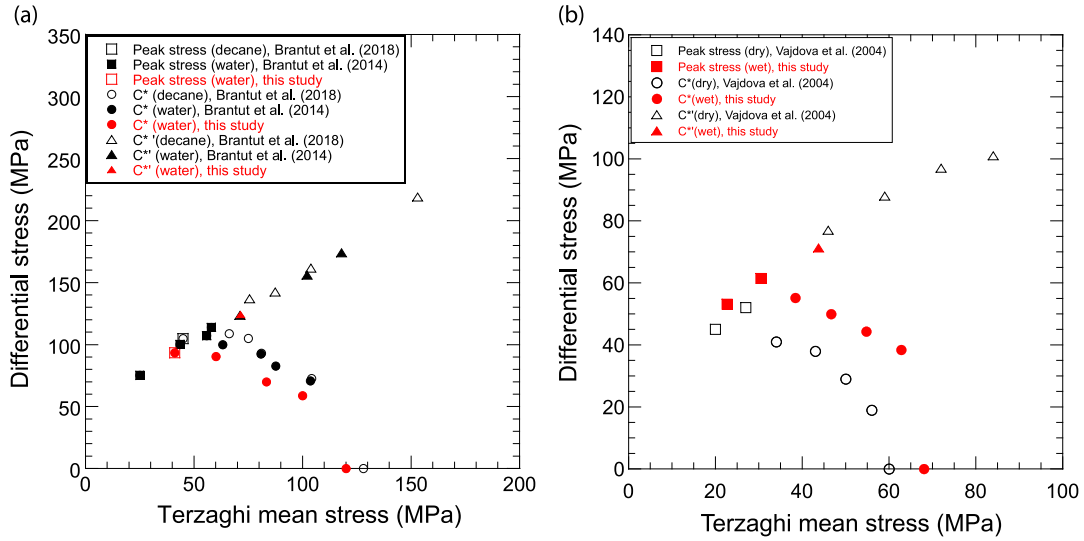

Figure 19. Stress states C', C^*, $C^{*\prime}$, and peak stress shown in the stress space for (a) Purbeck and (b) Indiana limestones. The data obtained in this study are presented in red. For Purbeck limestone, the data of Brantut et al. (2014) for water-saturated samples and Brantut et al. (2018) for decane-saturated samples are presented as black closed and open symbols, respectively. For Indiana limestone, the data of Vajdova et al. (2004) on nominally dry samples are presented as black open symbols.

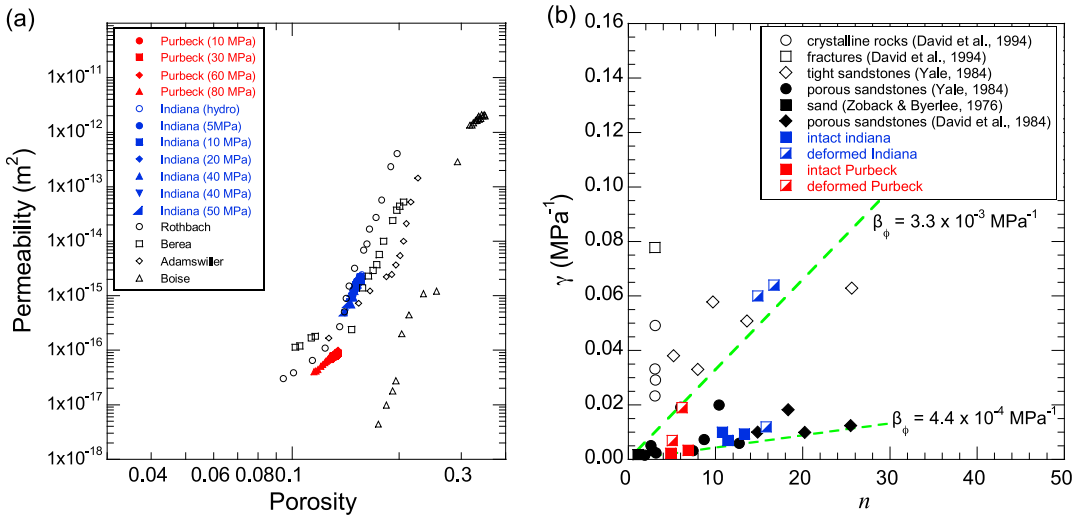

Figure 20. (a) Permeability as a function of porosity for the full set of data obtained in this study on Indiana (blue) and Purbeck (red) limestones. For reference, the data on four sandstones from David et al. (1994) are presented as open symbols. (b) Pressure sensitivity exponent γ as a function of the porosity sensitivity exponent n for deformed samples of Purbeck (red) and Indiana (blue) limestones. For reference, the theoretical predictions of equation (2) are presented as green dashed lines for two values of the pore compressibility β_ϕ. The data of sand in Figure 20 is referenced from Zoback and Byerlee (1976).

preexisting pores and dilatant microcracks in controlling the tortuosity (Zhu & Wong, 1996). Although such a model may indeed apply to our limestones, the interplay is expected to be complicated by the partitioning of pore space and transport between the macropores and micropores. Whether the additional complication results in the very low values of ξ observed in these limestones is a question that warrants further modeling study in the future.

In the transitional regime the interplay of compaction and dilatancy can be complicated. The initially compactive deformation may be transient in nature, ultimately leading to dilatancy at stress states beyond $C^{*\prime}$. Although this phenomenon has been widely observed in porous limestones (Vajdova et al., 2004), there is a paucity of data on the associated permeability evolution. Our data here (Figures 5b and 9) show that, similar to dilatant failure in the brittle faulting regime, permeability may increase or decrease in a dilating rock

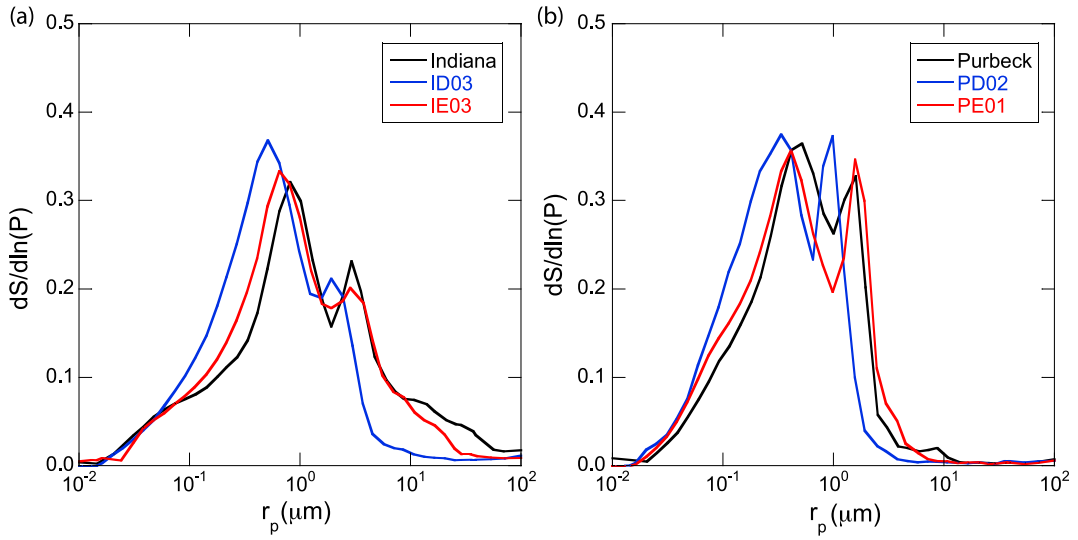

Figure 21. Effective pore throat diameter and the corresponding mercury capillary pressure as functions of cumulative pore space inferred from mercury injection tests on samples of (a) Indiana limestone: Undamaged (black) and triaxially deformed beyond C^* at effective pressures of 30 MPa (red) and 50 MPa (blue). (b) Similar data on samples of Purbeck limestone: Undamaged (black) and triaxially deformed beyond C^* at effective pressure of 80 MPa (red and blue).

Table 4
Permeability Change Factor ξ of Limestones

Sample	Initial porosity (%)	ξ	References
Purbeck	14.0	0.0178	This study
Oolithe blanche	15.7	0.1484	Regnet et al. (2015)
	15.3	0.11	
Indiana	15.7	0.0049	This study
	15.8	−0.0003	
Estaillades	28.1	−0.0211	Dautriat et al. (2011)

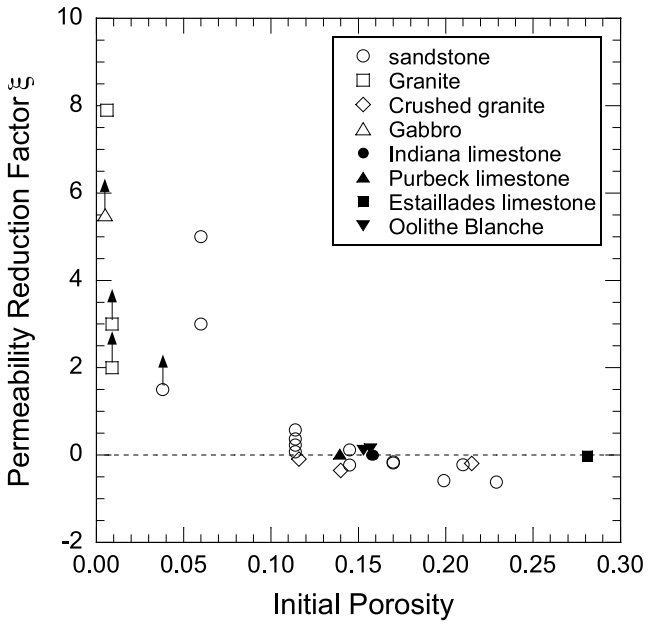

Figure 22. Relative change of permeability from the onset of dilatancy to the peak differential stress inferred in this study for Indiana (closed circles) and Purbeck (closed triangles) limestone. Values for Estaillades limestone and Oolithe Blanche inferred from the studies of Dautriat et al. (2011) and Regnet et al. (2015), respectively, are also given. For reference, values for sandstone (open circles), granite (open squares), crushed granite (open diamonds), and gabbro (open triangles) compiled by Wong and Zhu (1999) are also shown.

loaded beyond C*′. Our preliminary data for Purbeck and Indiana limestones show that the correlation between permeability and porosity changes is positive if the coefficient ξ is positive, and vice versa.

4.4. Pore Collapse and Related Damage Characterized by Mercury Porosimetry

To characterize quantitatively the partitioning of damage between macropores and micropores, for each limestone we performed mercury porosimetry on one hydrostatically compacted sample and one shear-compacted sample (Table 3). The equipment and experimental protocol were identical to Y. Wang et al. (2018), and for comparison their data for the undamaged limestone samples are also included in Figure 21. For each sample percentage volume S of the pore space intruded by mercury at the capillary pressure P was determined. To highlight the partitioning of macropores and micropores, we used the method suggested by Lenormand (2003) and plotted the nondimensional parameter $P\,\mathrm{d}S/\mathrm{d}P = \mathrm{d}S/\mathrm{d}\ln P$ as a function of the capillary pressure (and corresponding pore diameter) in Figure 21. The incremental area under this curve is proportional to the percentage volume of the pores associated with that pore throat diameter.

For either limestone, the pore throat distributions of both undamaged and damaged samples are bimodal. There is an overall trend for the distributions to shift to smaller pore sizes in the damaged samples. More significant shifts were observed in the two shear-compacted samples, particularly in the macropore range. In the Indiana limestone sample ID03, macropores with throat radius larger than 10 μm were basically eliminated (Figure 21). Such deformation can significantly reduce the conductances of throats that connect the macropores, but if the percolative transport is rate limited by the micropore networks, then the overall effect of macropore collapse on the permeability may not be large unless micropores are also eliminated in parallel. However, the mercury porosimetry data show that in the micropore range, even though the peak shifted to smaller throat radius in a damaged sample, overall there seems to be a uniform increase in the percentage volume for all micropore sizes, which may be related to microcracking associated with cataclastic collapse of macropores (Zhu et al., 2010). This implies that permeability contribution from the micropores may actually increase, and the trade-off is such that the significant porosity reduction primarily due to macropore collapse results in a relatively small permeability reduction, which is manifested by relatively small values of the coefficients n and γ for undamaged samples.

4.5. Effective Stress Behavior in a Limestone With Dual Porosity Homogenized by Damage

In a recent study, Y. Wang et al. (2018) systematically investigated the effective stress behavior of four water-saturated limestones with porosities ranging from 13% to 30%. Their measurements were conducted on undamaged samples, and we here conducted similar measurements on damaged samples of two of their limestones. A key conclusion of Y. Wang et al. (2018) is that, in these limestones with dual porosity, their effective stress coefficients for permeability and pore volume change were consistently greater than 1. This contradicts the behavior predicted for a microscopically homogeneous assemblage, with β, κ, and α all equal to or less than unity (Berryman, 1992a, 1992b; Walsh, 1981).

This apparent contradiction motivated Y. Wang et al. (2018) to circumvent the assumption of microscopic homogeneity and instead consider a model that differentiates explicitly the macropores and micropores. One such a model was originally formulated by Berryman (1992a, 1992b), which can capture more realistically

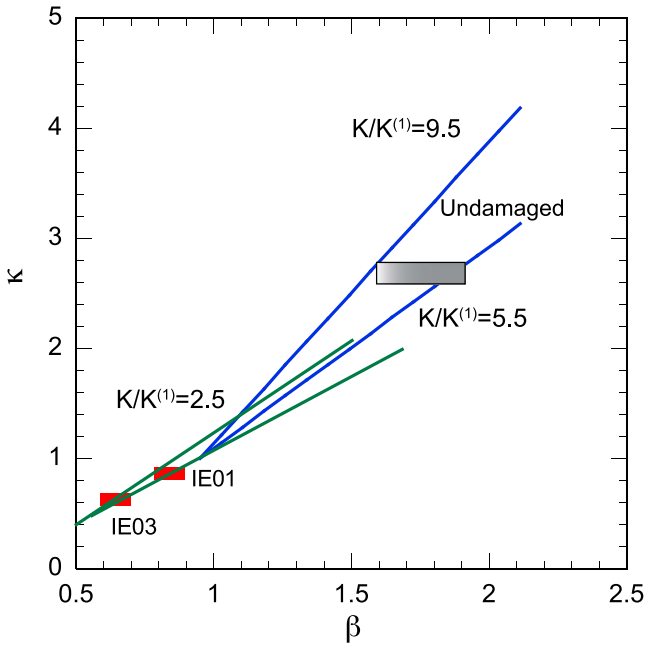

Figure 23. Effective stress coefficient for permeability κ as a function of effective stress coefficient for pore volume change β. The gray box indicates the data range found by Y. Wang et al. (2018) for undamaged limestones. These data could be bracketed by the theoretical predictions of Berryman's model (equations (S4a) and (S4b)) for values of $K/K^{(1)}$ between 5.5 and 9.5 (gray lines). The red boxes indicate the data ranges for sample IE01 deformed hydrostatically beyond $P^*$and sample IE03 deformed triaxially beyond C^*. Data for compacted Indiana limestone could also be bracketed using equations S4(a) and S4(b) with the same ratio $K/K^{(1)} = 2.5$, and $\alpha = 0.75$ and $\alpha = 0.55$ for IE01 and IE03, respectively.

the interplay of dual porosity in controlling the hydromechanical behavior. Y. Wang et al. (2018) modified this model and considered an assemblage of two distinct porous constituents: whereas constituent 1 is embedded with micropores and it provides an interconnected and percolative path for hydraulic transport, constituent 2 is isolated and embedded with macropores. Mercury porosimetry data (Figure 21) indicate that the throat size distributions of the initially undamaged and damaged samples are qualitatively similar and bimodal, which suggests that the effective stress behavior of our damaged samples can also be analyzed using the model. Details on the assumptions behind the model of Berryman (1992a, 1992b) as modified by Y. Wang et al. (2018), as well as its theoretical predictions are included here as supporting information Text S3 (Berryman, 1992a, 1992b; Berryman & Milton, 1991; Y. Wang et al., 2018).

Equations (S4a) and (S4b) were combined to analyze the effective stress coefficients of the undamaged and damaged samples of Indiana limestone (Figure 23). The range of β and κ values for an undamaged sample measured by Y. Wang et al. (2018) is indicated by the gray rectangle in the figure. The model predicts that the two coefficients are related in an approximately linear manner, and the laboratory data of undamaged samples can be bracketed by two lines that correspond to $K/K^{(1)}$ ratios of 5.5 and 9.5, where K and $K^{(1)}$ denote the bulk moduli of the rock and constituent 1 (with embedded micropores), respectively. The bulk modulus ratio is predicted to be relatively high, in the range used to model the effective stress behavior in a sandstone with high clay content (e.g., Al-Wardy & Zimmerman, 2004).

For our damaged samples, we used parameters identical to those of Y. Wang et al. (2018) listed in supporting information Text S3, except for the porosity and Biot coefficient. Given their damage history, for the total porosity and microporosity we used values smaller than those of Y. Wang et al. (2018) by 2% and 1%, respectively. It should, however, be noted that the overall behavior is not sensitive to this variation in porosities. Guided by our laboratory data, we used $\alpha = 0.75$ and 0.55 for IE01 and IE03, and the corresponding model predictions are shown in green and blue colors, respectively (Figure 23). Our data for the two samples are shown as red rectangles, which are bracketed by the two lines predicted by the model for a fixed modulus ratio of $K/K^{(1)} = 2.5$ (Figure 23). Not included here are data for IE02, which span a broad range of β values and can be fitted by the model only if we were to adopt very different values for the other parameters (n_1 and q).

A plausible explanation that the model requires the ratio $K/K^{(1)}$ to attain a value as low as 2.5 is that collapse of the macropores was accompanied by pervasive damage in the form of microcracks (Vajdova et al., 2012), which can effectively reduce the bulk modulus of constituent 2 and lead to an overall decrease of K for the bulk rock. Such cataclastic damage likely corresponds to the increase of relatively narrow throats indicated by mercury porosimetry in the damaged samples (Figure 21). If they develop extensively, the stress-induced microcracks may provide hydraulic paths that can effectively connect the macropores with the micropores, with two important implications. First, the assumption of Y. Wang et al. (2018) that the macropores can be idealized as isolated is invalid, and it is then moot to what extent their model is applicable to our damaged samples. Second, although the hydromechanical process on the grain scale involves the complex interaction of a multiplicity of macropores, micropores, and microcracks, this complex scenario may actually develop in a qualitatively similar manner at different sites throughout the rock sample. In this sense, the cataclastic damage may have homogenized the pore structure, rendering it unrealistic and unnecessary to separate the pore space into two distinct constituents. Accordingly, our damaged samples can be idealized as a spatially homogeneous aggregate made up of hybrid units of interconnected macropores, micropores, and microcracks. For such a microscopically homogeneous assemblage, the effective stress coefficients must

satisfy these inequalities (Berryman, 1992a): (1) the pore volume coefficient β is greater than or equal to the Biot coefficient α, which is greater than or equal to the total porosity ϕ; (2) both the permeability coefficient κ and pore volume coefficient β are less than or equal to 1. Indeed, our laboratory measurements are basically consistent with these inequalities, which suggests that stress-induced cataclastic damage in a limestone with dual porosity leads to an overall homogenization of the pore structure, such that its effective stress behavior can be approximated as microscopically homogeneous.

5. Conclusion

In this study, we investigated systematically the influence of inelastic deformation and failure mode on permeability of Indiana and Purbeck limestones, with porosities of 16% and 14%, respectively. Permeability measured during hydrostatic and triaxial compression showed comparable evolutions in both limestones under relatively high effective pressures. With the development of shear-enhanced compaction, a permeability reduction by up to factor 3 was observed. Overall, our data on permeability revealed smaller reduction of permeability due to inelastic compaction in limestones than that observed in sandstones. At relatively low effective pressures, dilatant failure was accompanied by a modest decrease and increase of permeability in Indiana and Purbeck limestones, respectively. Together with published data, this implies an overall trend for the correlation between porosity and permeability changes to switch from positive to negative with increasing porosity. A similar trend has also been observed in other porous and compact rocks.

Previous studies on both Indiana and Purbeck limestones also emphasized that these rocks are double-porosity medium with significant proportions of macropores and micropores. In the absence of a percolative backbone of macropores, micropores exert a significant influence its permeability. In this context, inelastic compaction by cataclastic pore collapse, preferentially of macropores, is not an efficient way to reduce significantly the permeability.

Previous measurements have confirmed that the effective stress behavior of limestone with dual porosity is different from the prediction for a microscopically homogeneous assemblage, in that its effective stress coefficients for permeability and pore volume change may attain values larger than 1. However, we showed that after a certain amount of inelastic compaction, both coefficients became less than 1. This means that the collapse of macropores had effectively homogenize the initially bimodal pore size distribution and that damaged limestone may be treated as a microscopically homogeneous assemblage.

Taken together with published material on the brittle-ductile transition in limestone (Brantut et al., 2014, 2018; Vajdova et al., 2004, 2012), our new data showed that in carbonate formations in the porosity range studied here, variations of both porosity and permeability associated to, for example, extraction of fluid are expected to be quite small if only mechanical compaction is involved. The occurrence of a transition from shear-enhanced compaction to dilatancy (C*′) revealed by laboratory experiments means that the porosity of rocks such as Purbeck and Indiana limestones cannot be significantly reduced by inelastic compaction alone. Our new data showed that these small variations of porosity are associated to permeability variations of less than one order of magnitude. These results have potentially important implications for 4-D reservoir monitoring in carbonate formations. In such context, our new results also suggest that the effective pressure coefficients for porosity change and permeability and their potential variations with inelastic compaction have to be taken into account.

Acknowledgments
We thank Xiaoqiong Wang for allowing us to use her data on the nitrogen-saturated sample of Indiana limestone and Christian David for providing us the permeability data on Oolithe Blanche limestones. This study was partially funded by the Hong Kong Research Grants Council GRF14323916, a Direct Grant of the CUHK Faculty of Science, the France-Hong Kong Collaborative Program Procore 30805PM and F-CUHK405/16, and by CNRS (PICS 07961). The first author's research at the China University of Petroleum-Beijing was funded by the National 973 Program (Grant 2015CB250903), National Science Foundation of China (Grant 51490652), and National Science and Technology Major Project (Grant 2017ZX05039004). The new data presented in this study are available on the website: *https://issues.pangaea.de/browse/PDI-17880*.

References

Al-Kharusi, A. S., & Blunt, M. J. (2008). Multiphase flow predictions from carbonate pore space images using extracted network models. *Water Resources Research*, *44*, W06S01. https://doi.org/10.1029/2006WR005695

Al-Wardy, W., & Zimmerman, R. W. (2004). Effective stress law for the permeability of clay-rich sandstones. *Journal of Geophysical Research*, *109*, B04203. https://doi.org/10.01029/02003JB002836

Baechle, G. T., Colpaert, A., Eberli, G. P., & Weger, R. J. (2008). Effects of microporosity on sonic velocity in carbonate rocks. *The Leading Edge*, *27*(8), 1012–1018. https://doi.org/10.1190/1.2967554

Baud, P., Exner, U., Lommatzch, M., & Wong, T.-f. (2017). Mechanical behavior, failure mode, and transport properties in a porous carbonate. *Journal of Geophysical Research: Solid Earth*, *122*, 7363–7387. https://doi.org/10.1002/2017JB014060

Baud, P., Reuschlé, T., Ji, Y., Cheung, C., & Wong, T.-f. (2015). Mechanical compaction and strain localization in Bleurswiller sandstone. *Journal of Geophysical Research: Solid Earth*, *120*, 6501–6522. https://doi.org/10.1002/2015JB012192

Baud, P., Rolland, A., Heap, M. J., Xu, T., Nicolé, M., Ferrand, T., Reuschlé, T., et al. (2016). Impact of Stylolites on the mechanical strength of limestones. *Tectonophysics*, *690*, 4–20. https://doi.org/10.1016/j.tecto.2016.03.004

Baud, P., Schubnel, A., Heap, M. J., & Rolland, A. (2017). Inelastic compaction in high porosity limestone monitored using acoustic emissions. *Journal of Geophysical Research: Solid Earth*, *122*, 9989–10,008. https://doi.org/10.1002/2017JB014627

Bauer, D., Youssef, S., Fleury, M., Bekri, S., Rosenberg, E., & Vizika, O. (2012). Improving the estimations of petrophysical transport behavior of carbonate rocks using a dual pore network approach combined with computed microtomography. *Transport in Porous Media*, *94*(2), 505–524. https://doi.org/10.1007/s11242-012-9941-z

Bauer, D., Youssef, S., Han, M., Bekri, S., Rosenberg, E., Fleury, M., & Vizika, O. (2011). From computed microtomography images to resistivity index calculations of heterogeneous carbonates using a dual-porosity pore-network approach: Influence of percolation on the electrical transport properties. *Physical Review E*, *84*(1), 01133. https://doi.org/10.1103/PhysRevE.84.011133

Berryman, J. G. (1992a). Effective stress for transport properties of inhomogenous porous rock. *Journal of Geophysical Research*, *97*(B12), 17,409–17,424. https://doi.org/10.1029/92JB01593

Berryman, J. G. (1992b). Exact effective-stress rules in rock mechanics. *Physical Review A*, *46*(6), 3307–3311. https://doi.org/10.1103/PhysRevA.46.3307

Berryman, J. G., & Milton, G. W. (1991). Exact results for generalized Gassmann's equations in composite porous media with two constituents. *Geophysics*, *56*(12), 1950–1960. https://doi.org/10.1190/1.1443006

Brantut, N., Baker, M., Hansen, L. N., & Baud, P. (2018). Microstructural control of physical properties during deformation of porous limestone. *Journal of Geophysical Research: Solid Earth*, *123*, 4751–4764. https://doi.org/10.1029/2018JB015636

Brantut, N., Heap, M. J., Baud, P., & Meredith, P. G. (2014). Mechanisms of time-dependent deformation in porous limestone. *Journal of Geophysical Research: Solid Earth*, *119*, 5444–5463. https://doi.org/10.1002/2014JB011186

Choquette, P. W., & Pray, L. C. (1970). Geologic nomenclature and classification of porosity in sedimentary carbonates. *American Association of Petroleum Geologists Bulletin*, *54*, 207–250.

Churcher, P. L., French, P. R, Shaw, J. C., & Schramm, L. L. (1991). Rock properties of Berea sandstone, Baker dolomite, and Indiana limestone. Paper presented at the SPE International Symposium on Oilfield Chemistry, Anaheim, CA. https://doi.org/10.2523/21044-MS

Coyner, K. B. (1984). Effects of stress, pore pressure, and pore fluids on bulk strain, velocity, and permeability of rocks. (PhD), Massachusetts Institute of Technology, Cambridge.

Dautriat, J., Gland, N., Dimanov, A., & Raphanel, J. (2011). Hydromechanical behavior of heterogeneous carbonate rock under proportional triaxial loadings. *Journal of Geophysical Research*, *116*, B01205. https://doi.org/10.1029/2009JB000830

David, C., Wong, T.-f., Zhu, W., & Zhang, J. (1994). Laboratory measurement of compaction-induced permeability change in porous rock: Implications for the generation and maintenance of pore pressure excess in the crust. *Pure and Applied Geophysics*, *143*(1-3), 425–456. https://doi.org/10.1007/BF00874337.

Fatt, I. (1958). Pore volume compressibilities of sandstone reservoir rocks. *Society of Petroleum Engineers, Transactions of the American Institute of Mining, Metallurgical and Petroleum Engineers*, *213*, 362–364.

Hart, D. J., & Wang, H. F. (1995). Laboratory measurements of a complete set of poroelastic moduli of Berea sandstone and Indiana limestone. *Journal of Geophysical Research*, *100*(B9), 17,741–17,751. https://doi.org/10.1029/95JB01242

Heffer, K. (2002). Geomechanical influences in water injection projects: An overview. *Oil & Gas Science & Technology–Revue IFENP*, *57*(5), 415–422. https://doi.org/10.2516/ogst:2002027

Ji, Y., Baud, P., Vajdova, V., & Wong, T.-f. (2012). Characterization of pore geometry of Indiana limestone in relation to mechanical compaction. *Oil & Gas Science and Technology –Revue IFENP*, *67*(5), 753–775. https://doi.org/10.2516/ogst/2012051

Ji, Y., Hall, S. A., Baud, P., & Wong, T.-f. (2015). Characterization of pore structure and strain localization in Majella limestone by X-ray computed tomography and digital image correlation. *Geophysical Journal International*, *200*(2), 701–719. https://doi.org/10.1093/gji/ggu414

Lenormand, R. (2003). Sca2003-52: Interpretation of mercury injection curves to derive pore size distribution. In Proceedings of 2003 International Symposium of SCA.

Lisabeth, H. P., & Zhu, W. (2015). Effect of temperature and pore fluid on the strength of porous limestone. *Journal of Geophysical Research: Solid Earth*, *120*, 6191–6208. https://doi.org/10.1002/2015JB012152

Paterson, M. S., & Wong, T.-f. (2005). *Experimental rock deformation—The Brittle Field* (2nd ed.). New York: Spinger.

Peacock, D. C. P., & Sanderson, D. J. (1995). Pull-aparts, shear fractures and pressure solution. *Tectonophysics*, *241*(1-2), 1–13. https://doi.org/10.1016/0040-1951(94)00184-B

Pittman, E. D. (1971). Microporosity in carbonate rocks. *AAPG Bulletin*, *55*, 1873–1878.

Regnet, J. B., David, C., Fortin, J., Robion, P., Makhloufi, Y., & Collin, P. Y. (2015). Influence of microporosity distribution on the mechanical behavior of oolithic carbonate rocks. *Geomechanics for Energy & the Environment*, *3*, 11–23. https://doi.org/10.1016/j.gete.2015.07.002

Sayers, C. (2008). The elastic properties of carbonates. *The Leading Edge*, *27*(8), 1020–1024. https://doi.org/10.1190/1.2967555

Tanino, Y., & Blunt, M. J. (2012). Capillary trapping in sandstones and carbonates: Dependence on pore structure. *Water Resources Research*, *48*, W08525. https://doi.org/10.1029/2011WR011712

Tondi, E., Antonellini, M., Aydin, A., Marchegiani, L., & Cello, G. (2006). The role of deformation bands, stylolites and sheared stylolites in fault development in carbonate grainstones of Majella Mountain, Italy. *Journal of Structural Geology*, *28*(3), 376–391. https://doi.org/10.1016/j.jsg.2005.12.001

Vajdova, V., Baud, P., & Wong, T.-f. (2004). Compaction, dilatancy and failure in porous carbonate rocks. *Journal of Geophysical Research*, *109*, B05204. https://doi.org/10.1029/2003JB002508

Vajdova, V., Baud, P., Wu, L., & Wong, T.-f. (2012). Micromechanics of inelastic compaction in two allochemical limestones. *Journal of Structural Geology*, *43*, 100–117. https://doi.org/10.1016/j.jsg.2012.07.006

Walsh, J. B. (1981). Effect of pore pressure and confining pressure on fracture permeability. *International Journal of Rock Mechanics and Mining Sciences*, *18*(5), 429–435. https://doi.org/10.1016/0148-9062(81)90006-1

Wang, Y., Meng, F., Wang, X., Baud, P., & Wong, T.-f. (2018). Effective stress law for permeability and deformation of four limestones. *Journal of Geophysical Research: Solid Earth*, *123*, 4707–4729. https://doi.org/10.1029/2018JB015539

Willemse, E. J. M., Peacock, D. C. P., & Aydin, A. (1997). Nucleation and growth of strike-slip faults in limestones from Somerset, U.K. *Journal of Structural Geology*, *19*(12), 1461–1477. https://doi.org/10.1016/S0191-8141(97)00056-4

Wong, T.-f., & Baud, P. (2012). The brittle-ductile transition in porous rock: A review. *Journal of Structural Geology*, *44*, 25–53. https://doi.org/10.1016/j.jsg.2012.07.010

Wong, T.-f., & Zhu, W. (1999). Brittle faulting and permeability evolution: Hydromechanical measurement, microstructural observation, and network modeling. In W. C. Haneberg, P. S. Mozley, C. Moore, & L. B. Goodwin (Eds.), *Faults and subsurface fluid flow in the*

shallow crust, *Geophysical Monograph Series* (Vol. 113, pp. 83–99). Washington, DC: American Geophysical Union. https://doi.org/10.1029/GM113p0083

Yale, D. P. (1984). Network modelling of flow, storage and deformation in porous rocks. (PhD thesis), Standford University, CA.

Yale, D. P., & Crawford, B. (1998). Plasticity and permeability in carbonates: Dependence on stress path and porosity. SPE/ISRM, 47582, 485–494. https://doi.org/10.2118/47582-MS

Zhu, W., Baud, P., & Wong, T.-f. (2010). Micromechanics of cataclastic pore collapse in limestone. *Journal of Geophysical Research*, *115*, B04405. https://doi.org/10.1029/2009JB006610

Zhu, W., & Wong, T.-f. (1996). Permeability reduction in a dilating rock: Network modeling of damage and tortuosity. *Geophysical Research Letters*, *23*(22), 3099–3102. https://doi.org/10.1029/96GL03078

Zhu, W., & Wong, T.-f. (1997). The transition from brittle faulting to cataclastic flow: Permeability evolution. *Journal of Geophysical Research*, *102*(B2), 3027–3041. https://doi.org/10.1029/96JB03282

Zoback, M. D., & Byerlee, J. D. (1976). Effect of high pressure deformation on permeability of Ottawa sand. *American Association of Petroleum Geologists Bulletin*, *60*, 1531–1542.